



mAbs



ISSN: 1942-0862 (Print) 1942-0870 (Online) Journal homepage: www.tandfonline.com/journals/kmab20

A unified topology-based classification of SARS-CoV-2 RBD neutralizing antibodies systematizes affinity trends across variants

Luis Fernando Cofas-Vargas, Paola Mendoza-Espinosa, Fernando D. Montalvo-Sandoval, Saumel Pérez-Rodríguez, Jesús Antonio Rauda-Ceja, Pablo Hernández-Peralta, Adrián Durán-Vargas, Mauricio A. Trujillo-Roldán, Norma A. Valdez-Cruz & Enrique García-Hernández

To cite this article: Luis Fernando Cofas-Vargas, Paola Mendoza-Espinosa, Fernando D. Montalvo-Sandoval, Saumel Pérez-Rodríguez, Jesús Antonio Rauda-Ceja, Pablo Hernández-Peralta, Adrián Durán-Vargas, Mauricio A. Trujillo-Roldán, Norma A. Valdez-Cruz & Enrique García-Hernández (2025) A unified topology-based classification of SARS-CoV-2 RBD neutralizing antibodies systematizes affinity trends across variants, mAbs, 17:1, 2575083, DOI: 10.1080/19420862.2025.2575083

To link to this article: https://doi.org/10.1080/19420862.2025.2575083

© 2025 The Author(s). Published with license by Taylor & Francis Group, LLC.	→ View supplementary material 🗹
Published online: 21 Oct 2025.	Submit your article to this journal
Article views: 161	View related articles 🗹
View Crossmark data 🗹	



REPORT

OPEN ACCESS Check for updates



A unified topology-based classification of SARS-CoV-2 RBD neutralizing antibodies systematizes affinity trends across variants

Luis Fernando Cofas-Vargas (Da.b.*, Paola Mendoza-Espinosa (Da.*, Fernando D. Montalvo-Sandoval (Dc.d.*, Saumel Pérez-Rodríguez (1)e, Jesús Antonio Rauda-Ceja (1)ad, Pablo Hernández-Peralta (1)f, Adrián Durán-Vargas nad, Mauricio A. Trujillo-Roldán o, Norma A. Valdez-Cruz o, and Enrique García-Hernández 102ª

alnstituto de Química, Universidad Nacional Autónoma de México, Ciudad Universitaria, Ciudad de México, México; Department of Biosystems and Soft Matter, Institute of Fundamental Technological Research Polish Academy of Sciences, Warsaw, Poland; Departamento de Bionanotecnología, Centro de Nanociencias y Nanotecnología, Baja California, México; de Posgrado en Ciencias Bioquímicas, Universidad Nacional Autónoma de México, Unidad de Posgrado, Edificio B, 1º Piso, Circuito de Posgrados, Ciudad Universitaria, Coyoacán, México; eBollyky Laboratory, Division of Infectious Diseases and Geographic Medicine, Department of Medicine, School of Medicine, Stanford University, Palo Alto, CA, USA; Facultad de Medicina Veterinaria y Zootecnia, Universidad Nacional Autónoma de México, Ciudad Universitaria, Ciudad de México, México

ABSTRACT

The receptor-binding domain (RBD) of the SARS-CoV-2 Spike protein, responsible for engaging the hACE2 receptor, is the principal target of neutralizing antibodies (NAb). To better understand how viral evolution undermines NAb protection, we present a comprehensive, topology-based classification derived from 544 NAbs and 60 nanobody-RBD complex structures. Five major NAb classes, each subdivided into two subclasses, were defined by binding zone, angle of approach, hACE2 competition, and hotspot usage. A systematic mapping of NAb-antigen contacts revealed 91 recurrent hotspot residues, some of which remain fully conserved across all Omicron variants. Leveraging > 2,300 experimentally dissociation constants spanning the Wuhan strain and Omicron lineages, we conducted a comparative affinity analysis across subclasses. NAbs in classes 1-3, which overlap the receptor-binding site, show progressive loss of affinity against Omicron, with many failing to bind recent subvariants due to emergent steric clashes and limited affinity maturation against the ancestral Wuhan RBD. Nonetheless, cases of Abs exhibiting resilience to viral drift have been documented. In contrast, classes 4 and 5 maintain high affinity regardless of their initial affinity for parental strains. Contemporary in-silico epitope predictors captured only ~40% of experimentally defined hotspots, highlighting the need for structure-guided approaches. By introducing a refined topological segmentation of the RBD grounded in previously described but unsystematized regions, our classification captures a broad diversity of NAb binding modes and provides an integrative structural framework that harmonizes prior classification schemes, its relationship with circulating variants, and highlights conserved epitope features relevant to broad-spectrum vaccine and therapeutic NAb design.

ARTICLE HISTORY

Received 13 August 2025 Revised 8 October 2025 Accepted 9 October 2025

KEYWORDS

Affinity evolution; antibody classification; epitope mapping; neutralizing antibodies; receptor binding domain

Introduction

COVID-19 is a severe acute respiratory syndrome caused by the coronavirus SARS-CoV-2, which had claimed nearly 7 million confirmed lives by July 2025¹. Classic symptoms include fever, cough, and shortness of breath, although their prevalence and severity vary among different viral variants^{2,3}. Thanks to an unprecedented global effort, vaccines based on DNA-plasmid, mRNA, recombinant protein, and nanoparticles were authorized between 2021 and 2025⁴⁻⁷. At the same

CONTACT Norma A. Valdez-Cruz 🔯 adri@ens.cnyn.unam.mx 🗊 Departamento de Bionanotecnología, Centro de Nanociencias y Nanotecnología, Universidad Nacional Autónoma de México, Km 107 Carretera Tijuana – Ensenada Apdo Postal 14, Ensenada, BC CP. 22800, México; Enrique García-Hernández 🔯 egarciah@unam.mx 🖃 Instituto de Química, Universidad Nacional Autónoma de México, Cudad Universitaria, Ciudad de México 04510, México

*These authors contributed equally.

Supplemental data for this article can be accessed online at https://doi.org/10.1080/19420862.2025.2575083

© 2025 The Author(s). Published with license by Taylor & Francis Group, LLC.

This is an Open Access article distributed under the terms of the Creative Commons Attribution-NonCommercial License (http://creativecommons.org/licenses/by-nc/4. 0/), which permits unrestricted non-commercial use, distribution, and reproduction in any medium, provided the original work is properly cited. The terms on which this article has been published allow the posting of the Accepted Manuscript in a repository by the author(s) or with their consent.



time, the isolation and characterization of neutralizing antibodies (NAbs) elicited by infection or vaccination have become foundational for understanding immune protection and guiding the development of new therapies and vaccines. Thus, a consistent pattern emerged across five years of research, revealing a convergence between immune responses and discovery of innovative therapeutic strategies.

The primary target of these NAbs is the SARS-CoV-2 Spike glycoprotein (S protein), which plays a crucial role in viral entry into host cells⁸. Since the emergence of the original Wuhan lineage in 2019, SARS-CoV -2 has followed an evolutionary trajectory marked initially by a gradual, and subsequently by a rapid and extensive, accumulation of mutations in the receptor-binding domain (RBD) of the S protein. Up to the appearance of Delta, most variants carried no more than four changes in the RBD (e.g., N501Y in Alpha; K417N/E484K/N501Y in Beta; L452R + T478K in Delta)9, resulting in only moderate escape from NAbs elicited by Wuhan-based vaccines. A considerable antigenic leap occurred with Omicron BA.1, which introduced 15 RBD residue substitutions, 11 of which were within the receptor-binding motif (RBM), reducing post-vaccination neutralization titers by more than 25- to 40-fold. Subsequent Omicron diversification (BA.2, BA.2.12.1, BA.4/5) introduced convergent changes, such as L452Q/R, F486V, and the reversion R493Q, which weaken or abolish binding of NAbs while compensating for affinity through N501Y or other adjustments¹⁰. Throughout 2023-2024, recombinant lineages (XBB) and subvariants (BQ.1, BA.2.86, JN.1, and XFG) converged on recurrent residue changes at positions 346, 452, 456, 486, and 493, deepening immune escape and compromising most available therapeutic NAb cocktails¹¹. This evolution reflects a tradeoff between immune evasion and maintenance of viral fitness: mutations that diminish receptor binding are often accompanied by compensatory substitutions that restore the interaction. Identifying conserved epitopes outside the RBM and adaptive paratopes tolerant of these convergent substitutions, therefore, stands out as a key strategy for developing vaccines and NAbs that can outpace future coronavirus waves.

The S protein is a homotrimer. Each protomer is initially synthesized as a single polypeptide and subsequently cleaved by host proteases into two functional regions: the N-terminal S1 subunit (residues 14-685) and the C-terminal S2 subunit (residues 686-1273). The S1 subunit mediates binding to the human angiotensin-converting enzyme 2 (hACE2), while the S2 subunit facilitates fusion of the viral and host-cell membranes. Each of the three S1 subunits contains an RBD, whose position is highly dynamic¹². The RBD adopts two principal conformations, "down" (closed) and "up" (open), that regulate its accessibility to hACE2 and are therefore key to understanding viral recognition and entry (Figure 1(A)). In the down conformation, the RBD is folded against the trimer core, partially occluding the receptor-binding site (RBS); this arrangement likely contributes to immune evasion or spatial regulation of receptor engagement 12-14. All three S1 subunits are tightly packed, with extensive inter-domain contacts stabilizing the overall structure. In the up conformation, one or more RBDs pivot outward from the trimer core, fully exposing the hACE2-binding surface and enabling receptor interaction. In the functionally active state, the virus is more vulnerable, as it exposes epitopes to potential NAbs. Structural studies indicate that the transition from a fully closed (all RBD-down) to a fully open (three RBD-up) trimer proceeds through intermediate states, wherein one or two RBDs adopt the up conformation, suggesting a stepwise activation mechanism¹⁵. At its core, the RBD features a twisted, five-stranded antiparallel β -sheet (β_1 - β_4 , β_7), which confers rigidity and structural support 16 (Figure 1(B)). This β -sheet is flanked by short α -helices (α_1 - α_8) and connecting loops. The RBM is situated between strands β_4 and β_7 and occupies the distal region of the RBD, forming a concave surface complementary to the N-terminal helix of hACE2.

The RBD has been partitioned into distinct topological zones (Figure 1(C))^{17,18}. Here we propose a detailed partition of the RBD, also based on the topological zone framework, with the residue composition of each region specified in Figure 1. The uppermost part of the RBM comprises three main regions: the "peak" (formed by the loop spanning residues 472–489), the "valley" (including the antiparallel strands β5 and β6), and the "mesa" (loops connecting α_7 – β_5 and β_6 – α_8). Additionally, the RBD presents two broad lateral regions: an "outer face," partially accessible when the RBD is in the down conformation, encompassing the α_1 - α_2 helices and the β_1 strand; and an "inner face," buried within the trimeric core in the closed S protein conformation, composed of residues from the β_2 to α_4 segment, and the α_5 , α_6 , and α_8 helices. Just beneath the mesa region, there is a descending region termed the "short cliff," which encompasses the α_3 and α_7 helices. On the opposite flank, beneath the peak region, begins the "long cliff," which includes part of the β_3 strand, the α_6 - β_4 connecting loop, the C-terminal end extending from the final portion of the β_7 strand, and the β_5 - β_6 loop (part of the RBM). The

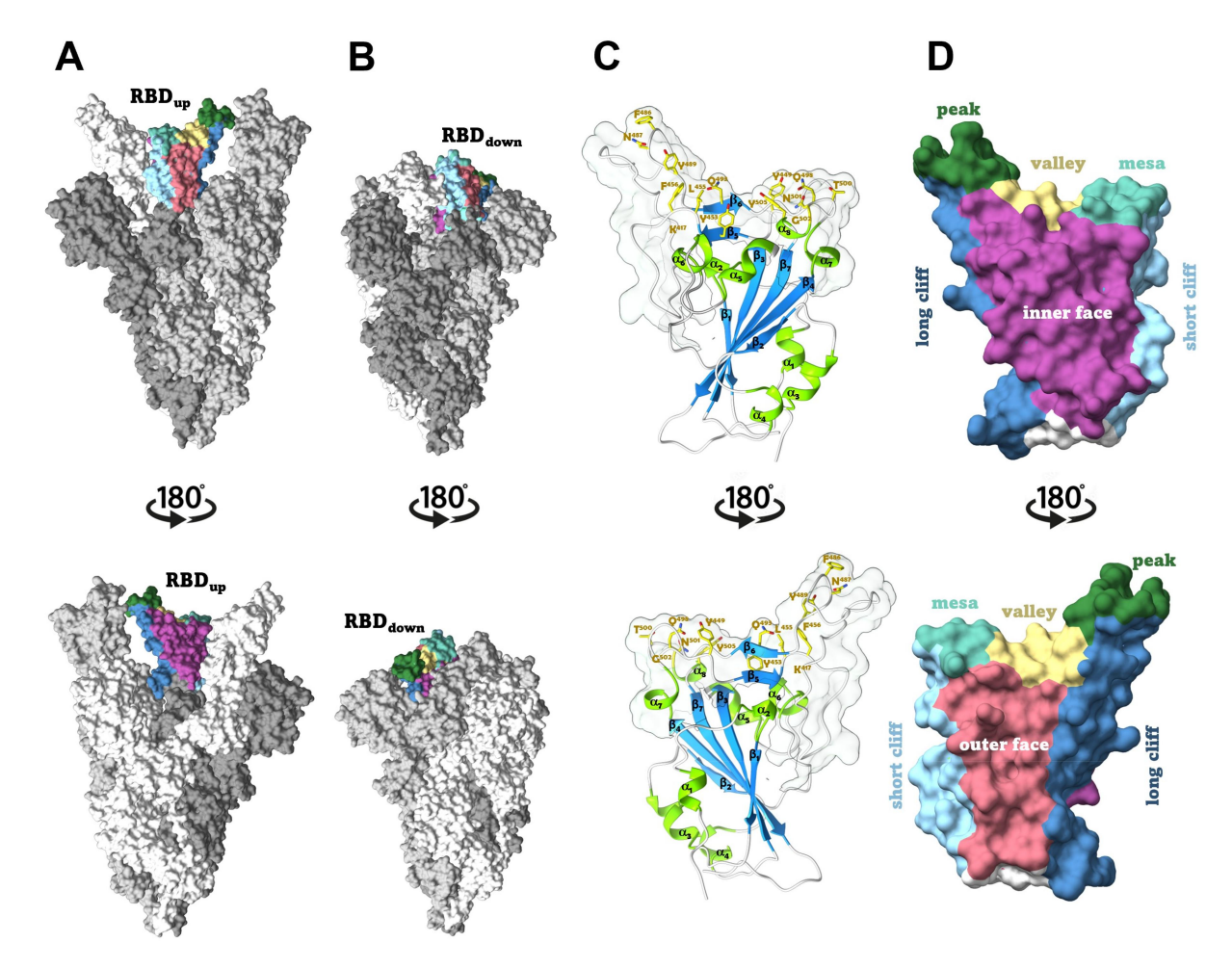


Figure 1. Spike protein and RBD structures. Representation of the homotrimeric S protein structure in fully open (A) and fully closed (B) conformations. One of the RBDs is colored as in panel D. C. Secondary structural elements (ribbons) and RBS region (yellow sticks) within the RBD. The RBM (residues 424-494) is highlighted by a transparent surface. The residue number ranges corresponding to the α-helices and the seven β-strands present in the RBD are α_1 (338–343), α_2 (350–352), α_3 (365–371), α_4 (384–387), α_5 (404–409), α_6 (417–421), α_7 (439–442), α_8 (503–505), and β_1 (354–358), β_2 (376–379), β_3 (394-403), β_4 (432-437), β_5 (452-454), β_6 (492-494), β_7 (507-516). D. Topological regions of the RBD, defined to facilitate the description of the Ab class binding zones. Residues composing each region are as follows: peak (472-489); valley (449-456, 490-495); Mesa (444-448, 496-500); short cliff (362-374, 436-443,506,509); long cliff (353,355, 393-396,426-432, 457-471, 514-523); outer face (333-352, 354, 356-361,397,399); inner face (375-392, 404-425, 433, 435, 501–505, 508); RBS (417, 449, 453, 455, 456, 486, 487, 489, 493, 498, 500–502, 505); RBM (403–507).

RBS comprises 14 residues spanning the peak, valley, mesa regions, and the upper portion of the inner face. The specific residue composition assigned to each topological region is detailed in the legend of Figure 1.

Functionally, NAbs fall into two main categories based on their ability to compete with hACE2: those that directly block the RBS and those that neutralize through alternative mechanisms, such as conformational interference, restriction of S protein motion, or Fc-mediated effector functions 19,20. Based on the recognition region of the RBD, Barnes et al. introduced a useful classification of NAbs²¹. This framework defines four classes based on the Ab's orientation relative to the RBD, its compatibility with the "up" and "down" RBD conformations within the S trimer, and the degree of overlap with the hACE2-binding site. Subsequent structural and competition studies revealed that subtle variations in binding angles within each class give rise to distinct subclasses, prompting the development of alternative antigen-centric approaches¹⁷. Up to now, however, there is no unified, structure-driven classification of anti-RBD NAbs. To address this gap, we conducted a comprehensive survey of RBD-binding NAbs whose complexes have been deposited in the Protein Data Bank (PDB). By systematically mapping Ab-antigen contacts, we (1) pinpointed the residue "hotspots" most frequently engaged across the entire database, (2) defined a set of recurring binding modes that encompasses prior classification systems, and (3) traced, in human NAbs, how each mode

tolerates or is compromised by the extensive mutations found in the Omicron lineage. Taken together, our framework unifies existing classifications, rationalizes differential neutralization across variants, and provides a basis for guiding future therapeutic and vaccine development efforts against current SARS-CoV-2 variants and potential future coronavirus outbreaks and pandemics.

Materials and methods

Collection of experimental S-protein/RBD-NAb complexes

A comprehensive search of the PDB was conducted to identify experimental structures of the SARS-CoV-2 S-protein/RBD complexed with NAbs, available as of January 2025, with a resolution better than 4.5 Å. This search retrieved a total of 540 PDB entries. In cases where multiple structures were available for a given NAb-RBD complex, the entry with the highest resolution was selected for analysis. When a structure contained more than one NAb, individual antigen-NAb pairs were isolated. This selection process resulted in a dataset comprising 556 unique antigen-NAb complexes compiled in our Master Table (Table SI-1). In addition, 60 nanobodies (Nb) bound to the RBD were retrieved. Because of the structural similarity, engineered Ab fragments were considered in the Nb group.

NAb classification

The collection of antigen-Ab complexes was structurally aligned using the conformation of the RBD bound to hACE2 as a reference (PDB ID 6M0J)¹⁶. Following alignment, NAbs were categorized based on their topological positioning relative to the RBD, initially using the classification scheme previously outlined²¹. Once grouped according to their binding regions, we further analyzed the local distribution patterns and angle of attack. In addition, we evaluated each NAb for its potential steric hindrance to hACE2 binding, exposure of epitopes in both the up and down conformations of the RBD in the S protein and possible clashes with spatially adjacent domains using reference structures PDB IDs 6VXX for the fully closed conformation²² and 6VSB for the completely open conformation of the S protein²³. Only the Fab region was considered when evaluating potential interference with hACE2 or adjacent domains, excluding the Fc region present in IgG structures from this analysis. Overall, this approach allowed further subdivision of NAbs into distinct subclasses and specific binding modes.

Analysis of intermolecular contacts

Interacting residue pairs at the interface of each protein complex were identified based on spatial and chemical criteria, as previously described²⁴, following the protocol reported²⁵. The interface of each S-protein/RBD-Ab complex was first analyzed using an enlarged van der Waals overlap criterion. To account for attractive dispersion forces, the van der Waals radii of heavy atoms were scaled by a factor of 1.24²⁶. Contacts were defined when the expanded atomic spheres of residues separated by more than four sequence positions overlapped. Next, we applied the repulsive Contacts of Structural Units (rCSU) criterion, which incorporates chemical and electrostatic parameters. A contact was classified as stabilizing if the number of attractive interactions exceeded that of repulsive interactions, ensuring chemically favorable contacts. This combined approach captures the dual nature of interfacial interactions, reflecting both steric packing and electrostatic complementarity.

RBD-NAb contact frequency

Contact analysis between the RBD and NAbs was carried out using a custom computational pipeline. Histograms were generated for each NAb subclass to represent contact frequencies for individual RBD residues, enabling a comparative analysis of contact patterns across all Ab groups. Residues exhibiting a contact frequency greater than 0.6 were designated as hotspots.

Paratope logos

NAb residues interacting with characteristic RBD hotspot residues of each subclass were identified. These contact compositions were then used to generate paratope residue logo plots employing Weblogo3²⁷.

Prediction of B-cell epitopes and antigenicity regions

The prediction of potential linear B-cell epitopes was performed using the BepiPred-2.0 server, available at DTU Health Tech (https://services.healthtech.dtu.dk/cgi). This tool enables residue-level evaluation across the RBD sequence. A threshold score of 0.5 was applied in BepiPred-2.0, consistent with the default configuration, with a specificity of 57% and a sensitivity of 59% (according to the performance metrics)²⁸. Residues scoring above this value were classified as potential epitope candidates²⁹. Furthermore, B-cell conformational epitopes (Discontinuous B-cell epitope prediction) were also predicted using the BepiPred-3.0 server, applying a threshold value of 0.22055³⁰.

Kolaskar and Tongaonkar antigenicity prediction, which aims to predict linear B-cell epitopes, was conducted using the semi-empirical approach³¹. This approach leverages the physicochemical properties of amino acid residues and is related to observed frequencies in experimentally validated epitopes. To identify potential antigenic regions, a sliding window of 10 consecutive amino acids was applied across the RBD sequence. For each window, an average antigenicity score was calculated based on the Kolaskar-Tongaonkar antigenic propensity scale. Regions exhibiting average scores exceeding the threshold value of 1.02 were classified as putative B-cell epitopes. This approach facilitates the pinpointing of peptide segments with a heightened likelihood of immune recognition. All computations were performed using custom scripts to automate antigenicity scoring and extract candidate epitope regions under the defined parameters.

Results

Topology-based classification of anti-RBD NAbs

In this work, an extensive analysis of the binding modes of NAbs targeting the RBD of SARS-CoV-2 allowed us to derive a new harmonized structural classification (Table 1). From a systematic study of available structural complexes of the RBD, NAbs were grouped into five main classes, subdivided further into a total of 10 subclasses. Each class was defined according to the specific RBD region (hotspot residues) recognized, the binding angle, and their ability to compete with hACE2. Classes 1 and 2 target predominantly residues of the RBS. Class 1 NAbs are characterized by extensive interactions with the RBS and an orientation toward the inner face of the RBD, making their binding compatible only with the up conformation of the RBD. This class is divided into subclasses 1A and 1B based on the extent and distribution of recognized RBS residues. Class 2 exhibits fewer contacts with the RBS and orientations toward the outer face of the RBD. Subclasses 2A and 2B differ in the specific RBD regions they contact, the degree of interference with hACE2, and the ability to bind the closed conformations of the S protein. Classes 3 and 4 interact with the short cliff region

Table 1. Structural classification of NAbs anti-RBD of SARS-CoV-2.

Class	Subclass	Interaction zone	RBD conformation	Ligand type
1	1A	Inner parts of peak, valley and mesa, upper regions of long cliff and inner face	Up	Competitive
	1B	Inner parts of peak and valley	Up	Competitive
2	2A	Outer face of peak and valley	Up/Down	Competitive
	2B	Upper and center regions of the outer face, upper regions of peak and long cliff	Up	Noncompetitive
3	3A	Mesa and top region of the short cliff	Up/Down, Up	Competitive
	3B	Mesa and top regions of the short cliff and the inner face	Up	Noncompetitive
4	4A	Top and middle regions of the inner face, middle of the short cliff	Up	Competitive
	4B	Bottom parts of the inner face and the short cliff	Up	Noncompetitive
5	5A	Middle region of the long cliff	Up	Noncompetitive
	5B	Middle region of the long cliff, middle of inner face	Up	Noncompetitive

of the RBD. Class 3 NAbs are grouped into subclasses 3A (competitive with hACE2) and 3B (noncompetitive). In contrast, class 4 NAbs bind to cryptic sites accessible only in the fully open conformation of the viral trimer, divided into subclasses 4A (competitive with hACE2) and 4B (noncompetitive). Finally, class 5 groups NAbs targeting the long cliff region of the RBD, which is largely inaccessible in the closed conformation of the S protein. These NAbs do not compete with hACE2 and are divided into subclasses 5A and 5B based on their extent of interaction with specific regions of the long cliff region. This classification facilitates a comprehensive understanding of the structural basis of the diverse neutralization mechanisms of NAbs against the RBD.

Class 1

The NAbs composing this class are characterized by extensive contact with RBS residues, with an angle of attack biased toward the inner face of the RBD, making their binding compatible only when the RBD is in the up conformation. Therefore, they are the NAbs that most closely mimic the binding mode of hACE2 (Figure 2). This class was further divided into two subclasses. Subclass 1A NAbs (n = 85, Table SI-2) interact extensively with the apical portion of the RBD, showing significant contact frequency with 26 residues (hotspots, contact frequency > 0.6), covering 12 of the 14 RBS residues (Figure 2(A,C)). These NAbs exhibit a remarkably uniform binding mode. The light and heavy chains overlap closely across the different NAbs, anchoring toward the peak and mesa regions, respectively. Tyrosine, serine, and glycine dominate among those residues with the highest frequency of contact with the RBD (Figure 2(C)). A similar usage of paratope

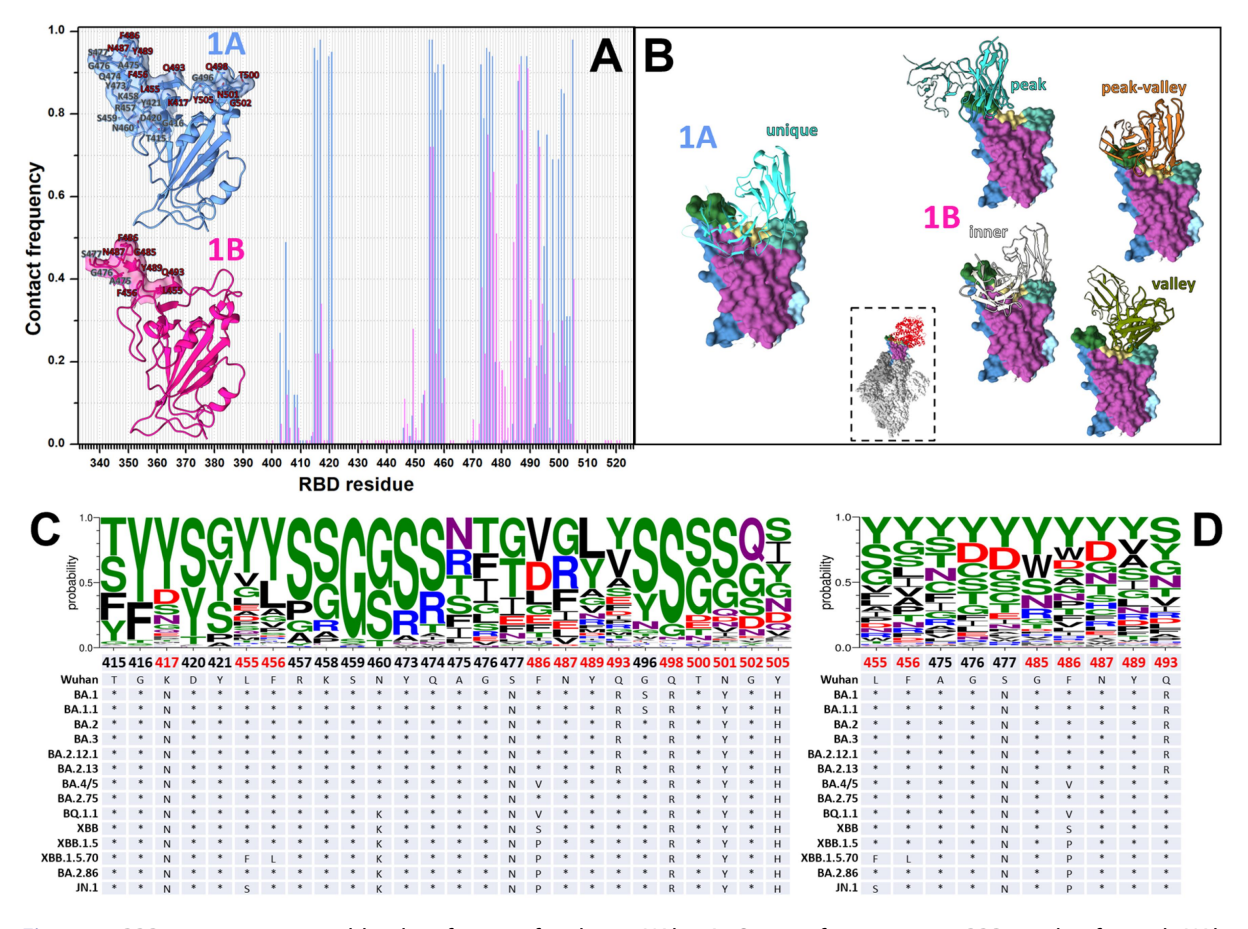


Figure 2. RBD contact zones and binding features for class 1 NAbs. A. Contact frequency per RBD residue for each NAb subclass. Surface representations of the RBD highlight hotspot residues (contact frequency ≥0.6), referenced to the Wuhan structure. RBS hotspots are in red font. B. Binding modes of subclasses 1A and 1B. Heavy and light antibody chains are depicted as thick and thin cartoon representations, respectively. The orientation of the NAb-bound RBD within the fulllength S protein structure is depicted in the dashed-line box. C,D. Paratope sequence logos for subclasses 1A and 1B, respectively, for hotspot positions in the RBD. The X-axis presents the RBD residue numbers, with Wuhan variant residues and substitutions observed across Omicron variants indicated below. RBD residues belonging to the RBS are in red font.



residues was observed across the other NAb classes (Figures 2–6). Of note is the high prevalence in the use of a glycine to interact with S^{459} , a highly conserved residue belonging to the long loop (residues 456–472) of the RBM which connects $\beta 5$ to the peak region, relatively distant from the RBS.

Subclass 1B NAbs (n = 138) primarily bind to a subset of 10 hotspot residues, seven of which belong to the RBS that 1A NAbs also bind to (Figure 2(A,D)). In addition, they interact with the RBS residue 485, which is scarcely recognized by subclass 1A. The intermolecular contact is made in a region that spans the inner parts of the valley and peak regions, with minimal interaction with the mesa region. These NAbs exhibit four binding modes, characterized by slightly different RBD contact residue preferences, although they generally maintain a similar angle of attack that is biased toward the inner face of the RBD (Figure 2(B), Table SI-3):

- (1) Peak binding mode (n = 69). In this predominant binding mode, NAbs are positioned primarily over the peak region, while making only marginal contact with the valley region. Residue 478 emerges as an additional hotspot unique in this mode.
- (2) Peak-valley binding mode (n = 39). In this binding mode, NAbs simultaneously contact both the peak and valley regions. While these NAbs use the same 10 overall subclass hotspots, they do so with higher frequency.
- (3) Inner face-shifted binding mode (n = 20). This binding mode is closer to the long cliff region, marginally contacting the valley region, and shifted toward the inner face. In this mode, residues 415, 417, 473, and 505 emerge as new hotspots, while the prevalence of residues 476, 477, and 485 is markedly reduced.
- (4) Valley binding mode (n = 10). This minor binding mode shows the highest overlap with the valley region. These NAbs feature a total of 16 hotspots, the highest among all binding modes within subclass 1B.

Seven Nbs were identified, all exhibiting binding modes that closely resemble those of the peak-valley subgroup of NAbs.

Class 2

This class binds to RBS residues less extensively than class 1. The NAbs anchor in a region oriented toward the outer face of the RBD (Figure 3). Two subclasses can be distinguished based on the specific region of the outer face to which they bind.

Subclass 2A NAbs (n = 86) bind to eight residues with significant frequency (Figure 3). Among these, residues 449 and 493, the only ones overlapping with the RBS, are among the most frequently contacted residues. Rather than directly targeting the RBS, they primarily engage the outer regions of the peak and valley regions, which are minimally contacted by hACE2 or class 1 NAbs. As a result, their angles of attack allow for binding to both the up and down conformations of the RBD. Nevertheless, because of their proximity to the RBS, they remain competitive with hACE2. Three distinct binding-mode clusters can be identified within this subclass (Table SI-4):

- (1) Valley-perpendicular binding mode (n = 52). This group of NAbs primarily binds to the valley region, positioning their two chains perpendicular to the antiparallel β 5- β 6 strands. They also contact the peak region and, to a lesser extent, with the mesa region. Many NAbs in this group feature an extended CDR3 loop, allowing them to invade the upper part of the inner face of the RBD. Despite being the most abundant binding mode, all these NAbs contact residue 449 (*frequency* = 1.0). In addition, they frequently interact with residues 446, 447, 450, and 492, which are not hotspots for subclass 2A as a whole. In contrast, residue 493 is contacted less frequently than the overall trend of this subclass.
- (2) Valley-parallel binding mode (n = 21). Unlike the previous binding mode, NAbs of this group bind parallel to the valley region and are further displaced toward the mesa region and the external face of the RBD. These NAbs make the most extensive contacts with the RBD among subclass 2A members, targeting 13 hotspots. Residues 345, 346, 440, 441, 444 and 445, located near the upper part of the short cliff region, are characteristic hotspots of this binding mode.

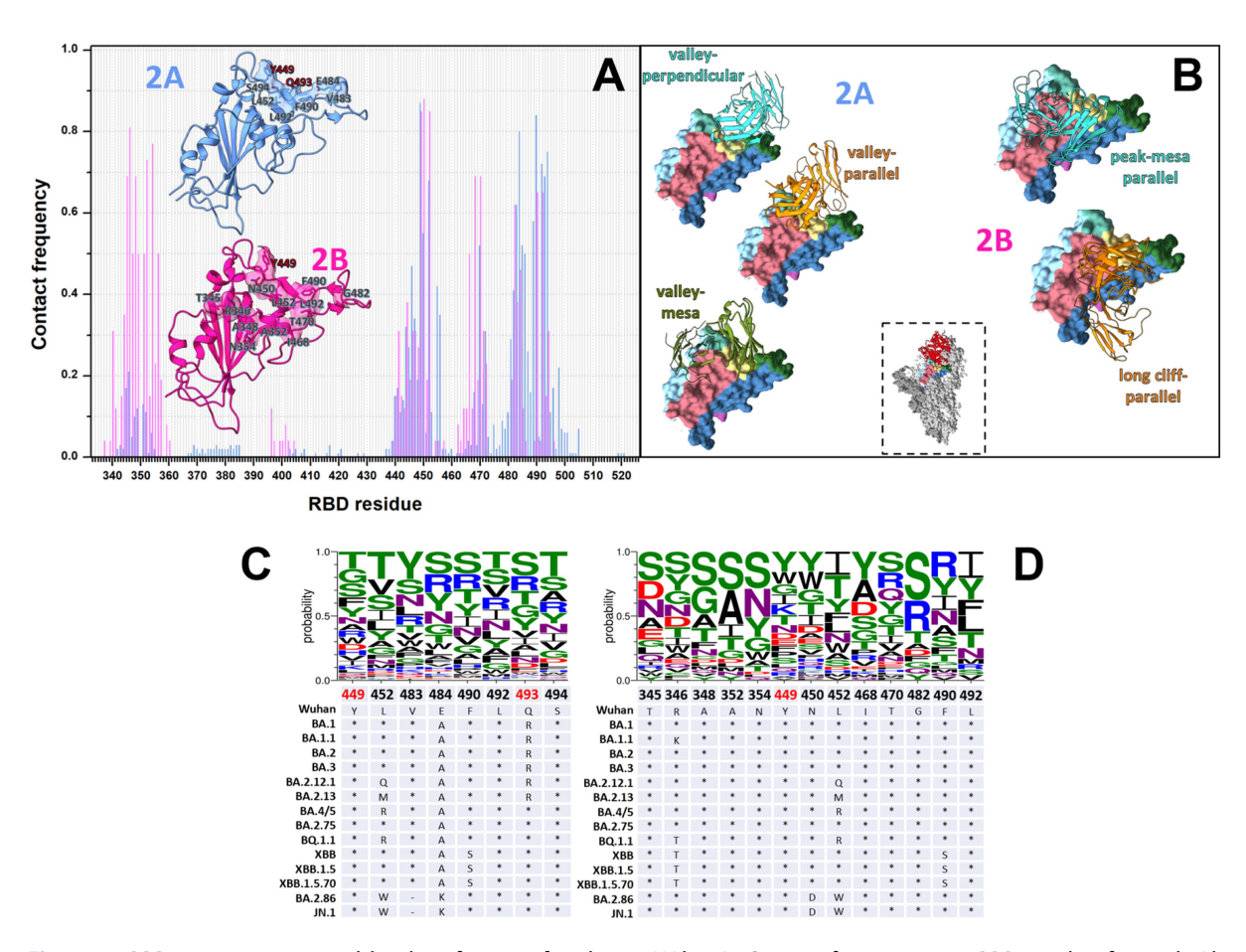


Figure 3. RBD contact zones and binding features for class 2 NAbs. A. Contact frequency per RBD residue for each Ab subclass. Surface representations of the RBD highlight hotspot residues (contact frequency ≥0.6), referenced to the Wuhan structure. RBS hotspots are in red font. B. Binding modes of subclasses 2A and 2B. Heavy and light antibody chains are depicted as thick and thin cartoon representations, respectively. The orientation of the NAb-bound RBD within the full-length S protein structure is depicted in the dashed-line box. C,D. Paratope sequence logos for subclasses 2A and 2B, respectively, for hotspot positions in the RBD. The X-axis presents the RBD residue numbers, with Wuhan variant residues and substitutions observed across Omicron variants indicated below. RBD residues belonging to the RBS are in red font.

(3) Valley-mesa centered binding mode (n = 13). NAbs in this mode also position their chains perpendicular to the valley. However, they are shifted toward the mesa region and the outer face of the RBD. Characteristic hotspots for this binding mode are residues 485, 486, and 489.

Subclass 2A includes 14 NAbs capable of simultaneously interacting with two RBDs. All these bivalent NAbs adopt a valley-perpendicular binding mode at their primary contact site. Five NAbs (C051, C144, C548, CLONE6, and S2M11) interact simultaneously with two RBDs in the down conformation. In these complexes, the secondary RBD contact is centered at the short cliff region (Figure 4(A)). The experimental structures reveal three NAb copies bound simultaneously, a unique property that enables them to stabilize the S protein in a fully closed conformation. The remaining nine bivalent NAbs (2H2, 5A6, BG1-24, BG7-20, C104, C121, DH1042, P5A-1B9, P17) are characterized by having an RBD in the down conformation as their primary binding site. In contrast, the secondary contact is established on the inner face of an RBD in the up conformation (Figure 4(B)). Except for C104, whose experimental structure exhibits only a single NAb copy bound bivalently, the other complexes additionally exhibit one or two NAb copies interacting monovalently. This implies that the primary RBD alone is sufficient to sustain their interaction.

Subclass 2A contains the largest number of Nbs among all subclasses, with a total of 30 members (Table SI-4). While all bind to the center of the valley region, they exhibit highly variable angles of attack. Notably, Nb B01, a synthetic construct consisting of three covalently linked human variable heavy domains, forms

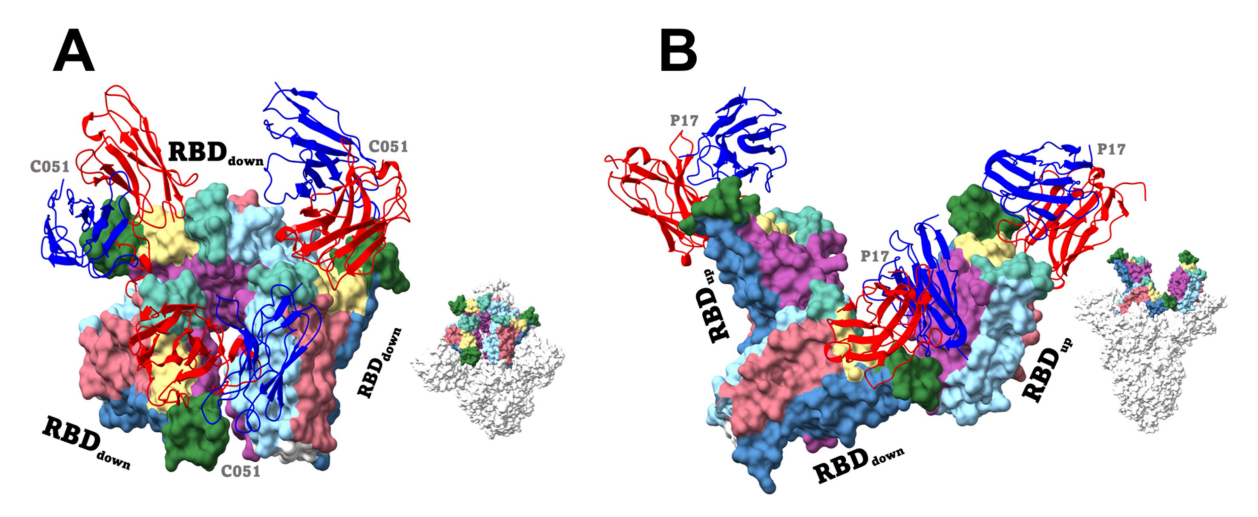


Figure 4. Bivalent subclass 2A NAbs. A. Example of a bivalent NAb (C051, PDB ID 7R8N³² engaging three RBD simultaneously, all in the down conformation. B. Example of a bivalent NAb (P17, PDB ID 7CWO³³) simultaneously bound to three RBD. One NAb molecule interacts with two RBDs, one in the down conformation (the primary binding site) and another in the up conformation (the secondary binding site). At the same time, the other two NAb copies each bind a single RBD in the up conformation. The relative orientations of the RBDs in the S protein are illustrated.

a bivalent RBD down/up contact via its N-terminal domain, while the other two domains establish monovalent interactions³⁴.

Unlike subclass 2A NAbs, those in subclass 2B (n = 21) do not obstruct hACE2 binding, as they target a region shifted toward the central portion of the external face of the RBD, which is solvent-exposed only in the up conformation (Figure 3). Despite this displacement, the RBS residue 449 remains a highly frequent contact point, albeit exclusively through its backbone. Two distinct binding modes can be identified within this subclass (Table SI-5):

- (1) Peak-mesa parallel binding mode (n = 13). This dominant binding mode arranges the two NAb chains parallel to the peak-valley-mesa axis, anchoring them at the central region of the external face with minimal interaction with either of the two cliffs. NAbs in this group share most of the hotspot residues characteristic of the entire subclass, with an increased frequency of contact in a zone below the valley and mesa regions.
- (2) Long-cliff parallel binding mode (n = 8). NAbs in this subgroup adopt a closely parallel orientation to the long cliff region, albeit with reduced overall contact. This positional shift decreases interaction with residues 345–349, which are characteristic of the peak-mesa parallel mode, while increasing contact with residues closer to the peak region.

Five Nbs were identified in this subclass, all exhibiting nearly superimposable binding poses centered close to the valley region.

Class 3

This class is characterized by binding to the short cliff, a solvent-exposed region regardless of the RBD conformation. Nevertheless, in some cases the angle of approach causes steric clashes between the NAb and adjacent RBDs, such that binding can only occur when the S protein adopts open or semi-open conformations. Based on their ability to compete with hACE2, these NAbs can be grouped into two subclasses. Subclass 3A (n = 39) binds close to the mesa region, targeting nine hotspot residues across the mesa and the top of the short cliff, including residue 500 of the RBS (Figure 5). Using the long axis of the short cliff as a reference, three distinct binding modes were identified (Table SI-6):

(1) Perpendicular binding mode to the short cliff (n = 26). The two NAb chains are positioned perpendicular to the short cliff and relatively close to the mesa region, sharing the same nine hotspots of the subclass 3A.

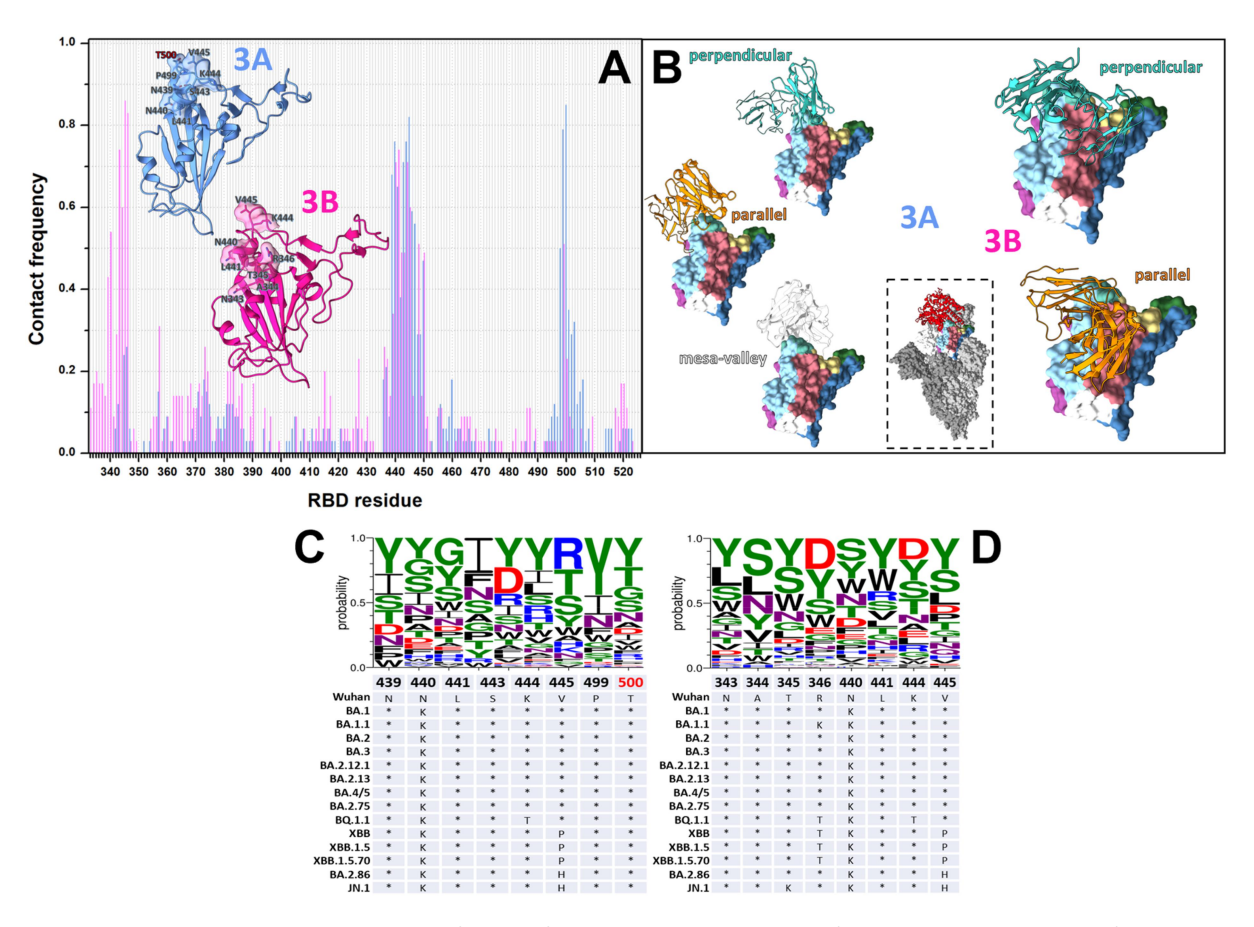


Figure 5. RBD contact zones and binding features for class 3 NAbs. A. Contact frequency per RBD residue for each Ab subclass. Surface representations of the RBD highlight hotspot residues (contact frequency ≥0.6), referenced to the Wuhan structure. RBS hotspots are in red font. B. Binding modes of subclasses 3A and 3B. Heavy and light antibody chains are depicted as thick and thin cartoon representations, respectively. The orientation of the NAb-bound RBD within the full-length S protein structure is depicted in the dashed-line box. C,D. Paratope sequence logos for subclasses 3A and 3B, respectively, for hotspot positions in the RBD. The X-axis presents the RBD residue numbers, with Wuhan variant residues and substitutions observed across Omicron variants indicated below. RBD residues belonging to the RBS are in red font.

- (2) Parallel binding mode to the short cliff(n = 10). The two chains of this subgroup of NAbs run parallel to the short cliff, also sharing the same hotspots of the subclass 3A as a whole, except for residues 439 and 440, which are used less frequently.
- (3) *Mesa-valley binding mode* (n = 3). These NAbs exhibit a binding mode almost exclusively on the mesa region, with minimal interaction with either face of the RBD.

Although the binding zone for subclass 3A remains solvent-exposed in the closed S protein conformation, the angle of attack is such that 11 perpendicular binding NAbs can only bind to an RBD in the down conformation if the neighboring RBD is not in a fully closed conformation (002-S21B10, 2–7, BETA-55, LY-COV1404, P2S-2E9, REGN10987, S2X324, TH272, THSC20. HVTR04, XG005, XGV264). In contrast, all NAbs binding parallel and 11 binding perpendicular to the short cliff can bind to the S protein in a fully closed conformation. Additionally, NAbs 812, BETA-24, BETA-54, HB27, XGV-286, and XGV-289, which are more displaced toward the mesa region and slightly inclined toward the inner face of the RBD, along with two of the perpendicular binding NAbs (6-2C and K288.2), can only bind to the RBD in its up conformation to avoid steric clashes with adjacent RBDs. In one of the structures of the 510A5 NAb, three copies of it were solved, forming bivalent contacts with the Wuhan variant S protein in a fully closed conformation. In this case, the primary site adopts a perpendicular binding mode to the short cliff, while the secondary site corresponds to the mesa binding mode, also of subclass 3A.

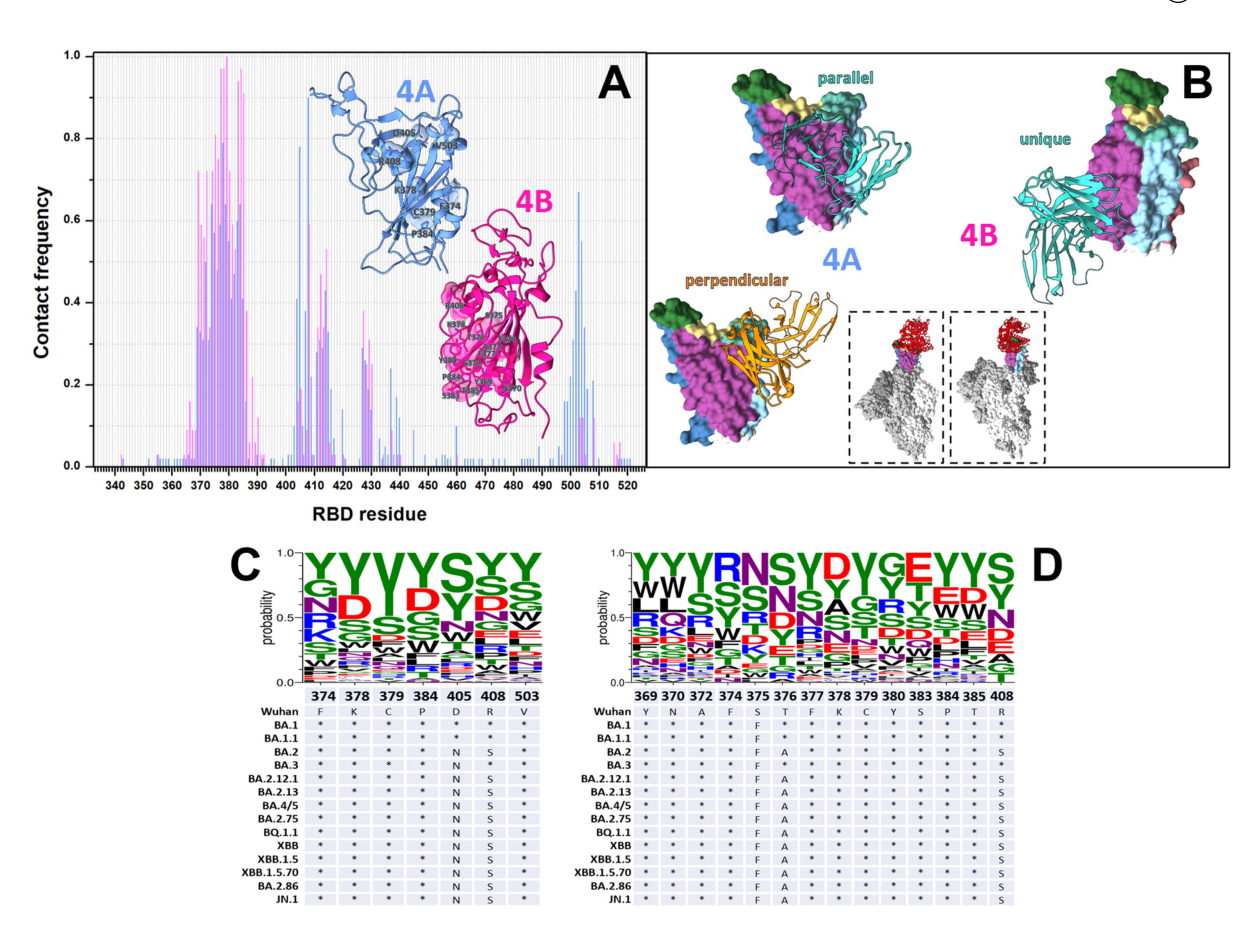


Figure 6. RBD contact zones and binding features for class 4 NAbs. A. Contact frequency per RBD residue for each Ab subclass. Surface representations of the RBD highlight hotspot residues (contact frequency ≥0.6), referenced to the Wuhan structure, B. Binding modes of subclasses 4A and 4B. Heavy and light antibody chains are depicted as thick and thin cartoon representations, respectively. The orientation of the NAb-bound RBDs within the full-length S protein structure are depicted in the dashed-line boxes. C,D. Paratope sequence logos for subclasses 4A and 4B, respectively, for hotspot positions in the RBD. The X-axis presents the RBD residue numbers, with Wuhan variant residues and substitutions observed across Omicron variants indicated below. RBD residues belonging to the RBS are in red font.

NAbs of subclass 3B (n = 35) also bind to a region near the short cliff of the RBD but shifted toward the inner face (Figure 5). Their eight hotspot residues are in a zone distant from the RBS, ensuring no interference with hACE2 binding. Like subclass 3A, the NAbs in this subclass can be grouped into two binding modes (Table SI-7):

- (1) Perpendicular binding mode to the short cliff (n = 27). The dominant binding mode of subclass 3B aligns the NAb chains perpendicularly to the long axis of the short cliff. This mode shares the same nine hotspots as the subclass 3B, but also frequently engages residues 448, 450, and 499.
- (2) Parallel binding mode to the short cliff(n = 8). This mode involves a parallel arrangement of the NAb chains relative to the long axis of the short cliff. Among the 10 hotspot residues in this subclass, four (343-346) are shared with subclass 3A, while the 334-340 region, located at the base of the short cliff, is uniquely utilized.

In addition, the Nb 3-2a2-4 was identified within subclass 3B.

Class 4

Like class 3, the interaction of these NAbs occurs in the short cliff region, but with a more pronounced binding bias toward the inner face of the RBD (Figure 6). Thus, the binding of these NAbs occurs at cryptic sites that are solvent-exposed only in the fully open conformation of the S protein.

Three of the seven hotspot residues in subclass 4A (n = 60) are relatively close to the mesa region, leading to competition with hACE2 binding (Figure 6(A)). Using the long axis of the short cliff as a reference, two binding modes can be distinguished (Table SI-8):

- (1) Parallel binding mode to the short cliff (n = 50). In this mode, NAbs position their heavy and light chains parallel to the short cliff, frequently extending the interaction toward the bottom of the short cliff. In addition to the seven hotspot residues of subclass 4A, this binding mode frequently contacts residues 377, 380, and 383.
- (2) Perpendicular binding mode to the short cliff (n = 10). In this mode, the interaction shifts toward the upper part of the short cliff and the inner face of the RBD. Despite their variable angles of attack, it is noteworthy that all these NAbs interact with residues 405 and 502–504.

Additionally, four Nbs were identified binding at the subclass 4A binding region, also causing steric clashes that hinder hACE2 binding (Table SI-8). One of these, 7A3, was solved with one of its three copies binding to the S protein in a bivalent interaction, engaging both an RBD in the up conformation and another in the down conformation³⁵. The secondary binding site corresponds to the subclass 2A region.

NAbs of subclass 4B (n = 24) target the lower region on the inner face of the RBD, without interfering with hACE2 binding (Figure 6, Table SI-9). This subclass exhibits a relatively constant binding mode, with the two chains positioned perpendicular to the long axis of the inner face. Its hotspot footprint comprises 14 residues, of which 13 constitute an almost continuous epitope within the 369–385 region. Except for H014³⁶, NAbs of this subclass require a fully open conformation of the S protein to avoid steric clashes with neighboring RBDs.

Eight Nbs have been solved bound to this region of the RBD (Table SI-9), including some, like 1–25 and S43, with demonstrated pan-sarbecovirus binding capacity^{37,38}. Sybody SR31 exhibits a unique binding mode, interacting closely with $\alpha 4$ and $\beta 2$, as well as with a region outside the RBD that includes residues $352-359^{39}$. This makes it the lowest-positioned epitope known on the RBD. Although SR31 lacks intrinsic virus-neutralizing ability, it has been tested as a fusion partner for competitive NAbs, leading to a mutual enhancement of affinity.

Class 5

This hACE2-noncompetitive class of NAbs targets the long cliff of the RBD, a region largely shielded from solvent by the N-terminal domain of an adjacent subunit when the S protein is in its closed conformation. Within this class, two distinct binding zones were identified. Subclass 5A NAbs (n = 10) primarily interact with the middle region of the long cliff, engaging nine hotspot residues, all of which show complete invariance throughout the evolutionary history of the analyzed Omicron variants (Figure 7). Although two distinct binding modes can be distinguished within this subclass – perpendicular (n = 7) and parallel (n = 3) to the short cliff – the number of complexes is still too small to derive statistically significant insights into the residue preference of each subgroup (Table SI-10). BN03 and 1–23 are the only Nbs documented in this region. BN03, a bispecific binder, also anchors through its CDRs to the region recognized by subclass 2A NAbs⁴⁰.

5B subclass NAbs (n = 16) establish fewer interactions with the middle and bottom portions of the long cliff region, instead adopting poses that extend toward residues located on the outer face of the RBD (Figure 7), collectively engaging 12 largely invariant hotspot residues. Of these NAbs, most (14) adopt a perpendicular orientation relative to the long cliff, while the remaining two are arranged parallel to it (Table SI-11). HSW-1 exhibits the ability to simultaneously bind two RBDs. Its primary contact is with an RBD in the up conformation, while its secondary contact is with an RBD in the down conformation, in the region recognized by subclass 2A NAbs. The Nb 2–10 has demonstrated broad cross-reactivity, binding with high affinity to several sarbecoviruses clades³⁷.

Binding affinity across Ab classes

Table SI-1 compiles a total of 2,360 dissociation constant (K_D) values from the literature, corresponding to the binding of the S protein or the isolated RBD by 534 distinct NAbs and Nbs. This extensive

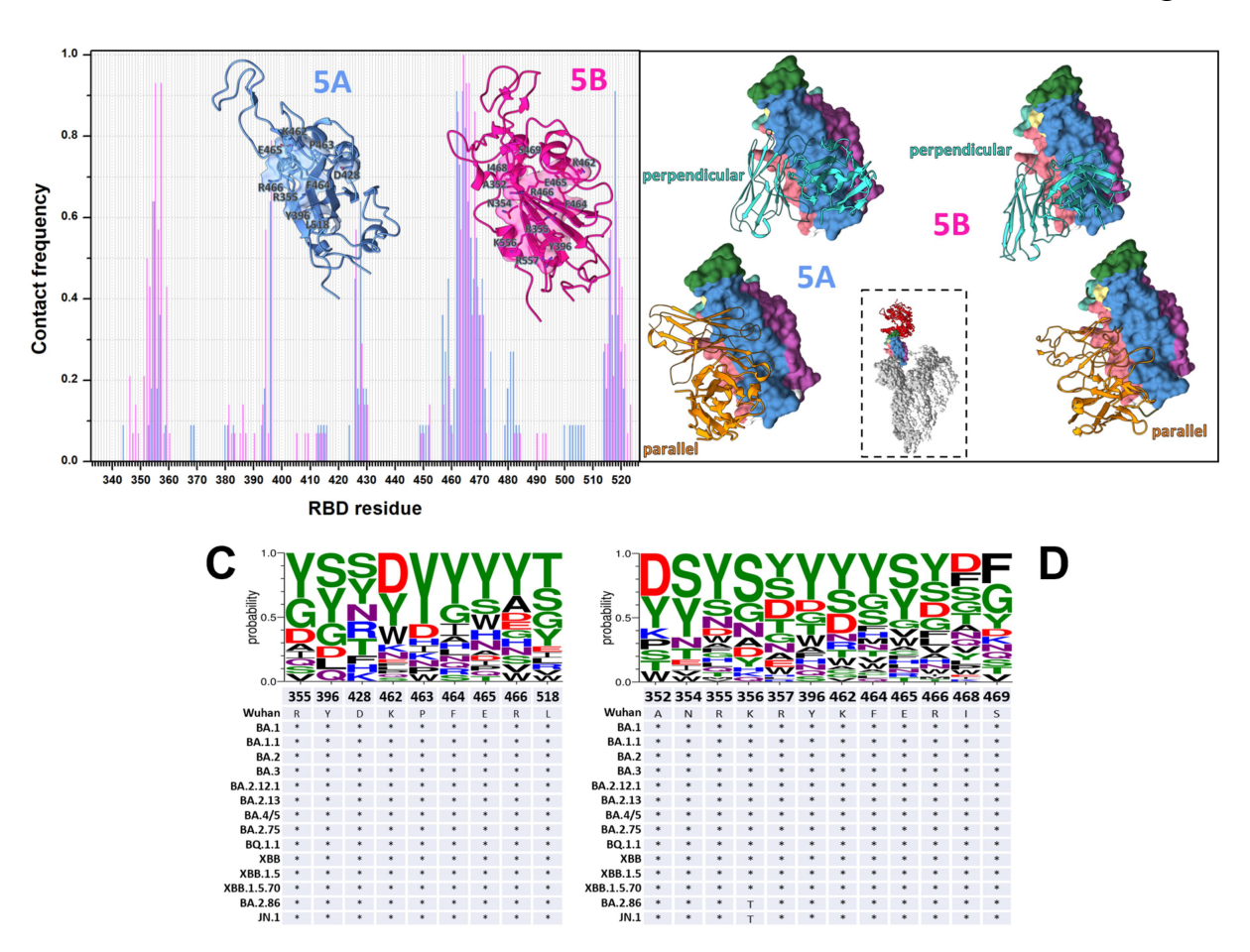


Figure 7. RBD contact zones and binding features for class 5 NAbs. A. Contact frequency per RBD residue for each Ab subclass. Surface representations of the RBD highlight hotspot residues (contact frequency ≥0.6), referenced to the Wuhan structure. B. Binding modes of subclasses 5A and 5B. Heavy and light antibody chains are depicted as thick and thin cartoon representations, respectively. The orientation of the NAb-bound RBD within the full-length S protein structure is depicted in the dashed-line box. C,D. Paratope sequence logos for subclasses 5A and 5B, respectively, for hotspot positions in the RBD. The X-axis presents the RBD residue numbers, with Wuhan variant residues and substitutions observed across Omicron variants indicated below. RBD residues belonging to the RBS are in red font.

dataset, mostly determined by surface plasmon resonance and biolayer interferometry, enables the analysis of global trends in the interaction strength of NAbs targeting the RBD of the SARS-CoV-2 S protein. To focus on naturally occurring human immune responses elicited by infection or vaccination, engineered and non-human derived NAbs were excluded from the analysis. Figure 8 displays the distributions of K_D values by subclass, measured against the Wuhan variant. All classes exhibit a similar K_D range, spanning from the sub- μ M order to extremely tight binders for which no measurable dissociation from antigen was observed. For reference, the K_D values for the interaction of the S protein and hACE2 fall within the 1–100 nM range^{41–47}. It is noteworthy that the fraction of high-to very high-affinity NAbs (K_D < 1 nM) is the majority in subclasses 1B, 3A, 4A, and 5A. Approximately half of the subclass 2B NAbs also exhibit high affinity. In contrast, weaker interactions are predominately found in subclasses 1A and 4B. For subclass 5B, the available data is still too scarce for a reliable comparison.

The analysis of K_D values against different Omicron variants revealed a heterogeneous landscape of sensitivity among the various NAb classes. However, the number of documented cases tracking affinity changes throughout the evolution of SARS-CoV-2 variants remains limited for some subclasses; therefore, the observed trends should be interpreted with statistical caution. Except for a few NAbs, affinity shifts have not been measured beyond the XBB variant until now. To exclude effects caused by large-scale conformational and dynamic changes in the S protein, the analysis focused on K_D values determined against the isolated RBD.

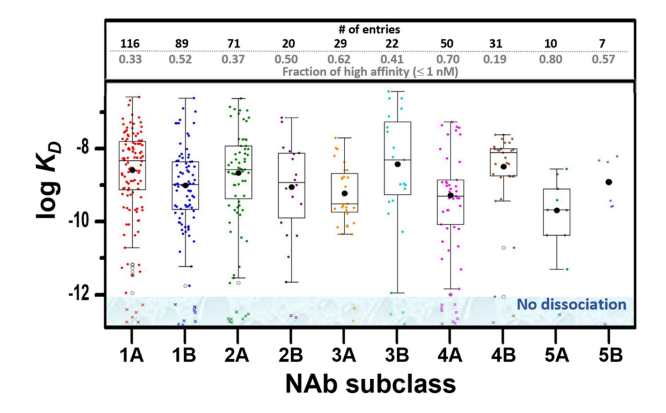


Figure 8. Distribution of binding affinities against Wuhan variant across anti-RBD/S protein NAb subclasses. KD values compiled from the literature are listed in Table SI-1. Data points corresponding to cases where no dissociation was observed are shown within the blue shaded area. These data were randomly positioned within the shaded zone to facilitate visual inspection. The number of K_D entries and the proportion of NAbs with high affinity ($K_D \le 1$ nM) in each subclass are indicated in the box at the top of the plot.

Based on the compiled affinity data in Figure 9, NAb classes 1 through 3 proved to be the most vulnerable to Omicron variants, with most members exhibiting significant losses in affinity or even loss of binding capacity. This sensitivity correlates with the fact that these classes recognize regions of the RBD that have accumulated the highest number of mutations over the course of viral evolution⁴⁸. Changes in hotspot residues tended to coincide with the loss of critical contacts or, more decisively, with the appearance of steric clashes. As a trend within these classes, NAbs that matured against the Wuhan variant with K_D values above 1 nM lost their ability to bind to Omicron variants, whereas those with higher affinity showed a greater likelihood of remaining active, albeit with decreased affinity. In contrast, classes 4 and 5 displayed notable resilience to the emergence of new variants, maintaining significant affinity in most cases regardless of their original binding strength. This behavior aligns with the fact that these classes recognize regions of the RBD characterized by lower mutational variability throughout the virus's evolutionary timeline (Figures 6 and 7).

In the case of subclass 1A, out of the 19 NAbs with affinity data available up to the XBB variant, only five retained binding capacity. Among them, BD55-1205 (Figure 9-(1A)) stands out for maintaining high affinity even against the JN.1 variant $(K_D = 0.69 \text{ nM})^{49}$. Of the eight RBD hotspot residues that changed relative to the Wuhan variant, residues 477, 486, and 498 are not contacted by this NAb, while residues 417 and 455 interact only with the backbone. In contrast, residues N501 and Y505, whose sidechains are in direct contact with the NAb, were substituted in all Omicron variants by Y and H, respectively, still maintaining favorable interactions with BD55-1205. Residue N460, which originally did not contact the NAb, was replaced by K starting in variant BQ.1.1, enabling the formation of an additional hydrogen bond, as revealed by the experimental structure with the RBD of the XBB.1.5 variant. Altogether, these changes were compatible with the preservation of BD55-1205 as a potent binder, even against recent viral variants. In contrast, some NAbs, such as COVA2-04, completely lost affinity starting with the first Omicron variant, partly due to the loss of interactions with key residues, including Y505⁵⁰. This early loss of recognition capacity coincided with a relatively low affinity maturation against the Wuhan variant. Notably, COVOX-158, which had undergone strong affinity maturation against the original strain, entirely lost binding capacity from variant BA.2.75 onward⁵¹. This loss correlates with the emergence of a severe steric clash caused by the N501Y substitution.

Like subclass 1A, NAbs belonging to subclass 1B largely lost their binding capacity against the more recent Omicron variants (Figure 9-(1B)). Of the seven NAbs with affinity evolution documented, only three retained binding ability up to the XBB variant. Notably, these NAbs had undergone strong affinity maturation against the Wuhan variant, and although their affinity weakened ($K_D > 1 \text{ nM}$) against Omicron variants, they remained functionally active. One such case is S2K146, which lost its ultrapotent character starting with the BA.1 variant, mainly due to the Q493R substitution⁵¹. This basic residue is bulky relative to the available space in the binding site and is positioned near another R, potentially generating substantial electrostatic repulsion. In the BA.4/5 variant, this change is reverted to Q. However, the F486V

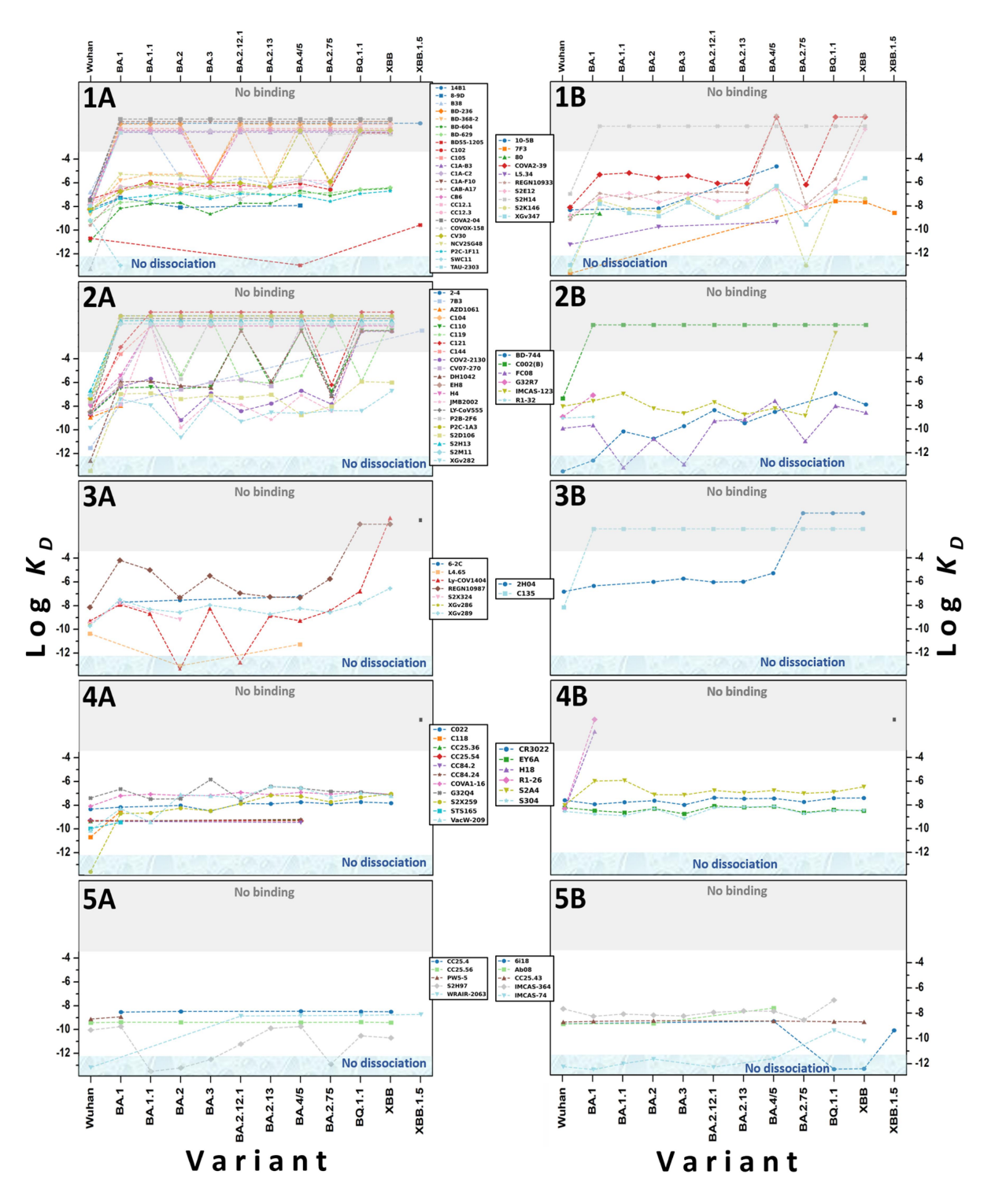


Figure 9. Evolution of binding affinities across Omicron variants in anti-RBD NAb subclasses. K_D values compiled from the literature are provided in supplementary Table SI-1. Only measurements corresponding to binding with the isolated RBD are included. Data points corresponding to no detectable binding and to cases where no dissociation was observed are shown within gray and blue shaded areas, respectively. These data were randomly positioned within the shaded zones to facilitate visual inspection.

mutation is introduced simultaneously, resulting in the loss of several hydrophobic contacts. Interestingly, in the BA.2.75 variant, where the F486V substitution is reverted, S2K146 regained its ultrapotent binding character. In contrast, the four NAbs that failed to bind to Omicron variants had undergone relatively modest affinity maturation against the Wuhan strain. One of them, S2H14, lost recognition beginning with



the BA.1 variant, correlating with the loss of interactions caused by the Q493R substitution⁵¹. Additionally, other mutations at positions that are not hotspot residues for subclass 1B proved even more detrimental to the NAb's binding affinity. For instance, the G496S, Q498R, and N501Y substitutions caused severe steric clashes, as well as the loss of a critical hydrogen bond due to the Y505H replacement.

Of the 19 subclass 2A NAbs tested for binding up to the XBB variant, only two retained detectable affinity (Figure 9-(2A)). Although DH1042 and S2D106 originally matured as ultrapotent NAbs against the Wuhan strain, their performance against Omicron subvariants differed markedly⁵¹. DH1042 exhibited a sharp loss of affinity, including complete binding loss against the BA.2.12, BA.4/5, and BO.1.1 variants. This decline is associated with the disruption of an intermolecular hydrophobic patch and a severe steric clash caused by the substitution of hotspot L452 with larger, polar residues. Although L452 was restored in the XBB lineage, binding remained impaired, apparently due to the hotspot F490S mutation, which disrupts the same hydrophobic interface. In contrast, S2D106 retained its binding capacity up to XBB, despite losing its ultrapotent character starting with BA.1. This initial decline in affinity appears to stem from electrostatic repulsion introduced by the hotspot Q493R mutation, which affects interaction with a positively charged residue in the NAb. Interestingly, aside from this single change, none of the other substitutions in Omicron variants, whether involving hotspot or non-hotspots residues, significantly perturbed the interaction with S2D106.

Starting with subclass 2B, the number of NAbs for which affinity evolution has been documented in response to Omicron variants decreases (Figure 9-(2B)). The region targeted by NAbs in this subclass corresponds to a semi-cryptic site, which displays lower hotspot variability compared to the subclasses discussed above. Among the four NAbs evaluated up to at least the BQ.1.1 variant, two lost their binding capacity, while the others exhibited reduced affinity, with affinity in the nM range. BD-744, initially an ultrapotent binder, weakened against the BA.1.1 variant, a change that correlated with the R346K substitution, which eliminates a hydrogen bond due to the shorter side chain⁵². Subsequent changes in affinity were partially, though not entirely, correlated with substitutions at position 452, the most variable hotspot within this subclass. In contrast to BD-744, FC08 did not initially mature as an ultrapotent binder but temporarily acquired such affinity against BA.1.1 and BA.3, without any detectable changes at contact residues that could explain these affinity variations⁵². However, substitutions at position 452 starting with BA.2.12.1 correlated with shifts in binding strength, including an increase in affinity upon reversion to the original leucine residue in BA.2.75, highlighting the importance of this hotspot in the affinity evolution of FC08.

Of the three subclass 3A NAbs whose affinity drift has been characterized (Figure 9-(3A)), only XGv289 retained binding capacity against XBB, which exhibited sub-nM strength against the Wuhan variant⁵¹. In contrast, Ly-COV1404 and REGN10987, which originally displayed low-to-mid nM affinities, lost their binding ability to the BQ.1.1 and XBB variants, respectively. The weakening of XGv289 against BA.1 and XBB coincides with the loss of interactions caused by the V445P and R498Q substitutions, respectively, while maintaining a stability plateau between BA.1 and BQ.1.1, consistent with conservation of the binding site. Regarding REGN10987, although no mutations in the RBD appear to cause direct steric clashes with this NAb, its affinity progressively declined across the Omicron lineage, eventually resulting in undetectable binding to BQ.1.1. In this context, the loss of affinity may be attributed to the disruption of the hydrogen bond coupled to the R436T substitution. Additionally, the K444T mutation leads to the loss of interactions with residues N44 and Y53 of the heavy chain. In contrast, the loss of binding capacity observed for Ly-COV1404 against XBB correlates with the introduction of steric clashes by the V445P substitution. These findings are consistent with previous reports showing that mutations at positions 346, 368, 399, 445, 446, 460, and 486 in Omicron variants compromise the neutralizing activity of several NAbs, including REG10987 and Ly-COV1404.

Subclass 3B is, to date, the least documented in terms of affinity evolution, despite the availability of 35 NAbs with solved structures in complex with either the isolated RBD or the full S protein. The two NAbs shown in Figures 9-(3B), which initially exhibited moderate binding affinity against the Wuhan variant, ultimately lost their binding capacity⁵¹. In the case of C135, this loss coincided with the N440K substitution found in the BA.1 variant, which introduces significant steric clashes that likely disrupted the interaction interface. In contrast, 2H04, whose loss of binding emerged only in the BA.2.75 variant, did not exhibit changes within its epitope, suggesting the involvement of long-range effects that may remodel the epitope's conformation.

NAbs from subclasses 4 and 5 clearly emerge as the most resilient among all groups analyzed. They break the trend observed in previous classes, where the decline in binding strength against Omicron variants largely depends on the degree of maturation originally achieved against the Wuhan strain. This behavior is explained by the fact that their epitopes are located in regions of the RBD that are less prone to mutation.

None of the two hotspot residues that vary within the epitopes of subclass 4A seem to significantly affect the interaction with any of the five NAbs in this subclass documented up to the XBB variant (Figure 9-(4A)). A noticeable change in affinity is observed in S2X259, where the D405N and R408S substitutions, present from the BA.2 variant onward, do not seem to significantly affect either the affinity or the molecular contacts formed⁵¹. In contrast, the S373P substitution, located outside the epitope region, may alter the orientation of the loop that contains it, affecting the arrangement of adjacent residues and thereby weakening the intermolecular interaction, which likely accounts for the loss of this NAb's ultrapotent character beginning with the BA.1 variant.

In the case of subclass 4B NAbs, H18 and R1-26 lose their binding capacity beginning with the BA.1 variant (Figure 9-(4B))⁵³. This loss appears to be associated with a backbone shift induced by the S373P substitution (Figure 10). Although residue 373 is not directly involved in interchain contact, the substitution disrupts interactions involving hotspot residues in the RBD's α 3 helix. In contrast, the four NAbs that maintain stable binding affinities, characterized by more skewed angles of attack toward α 4, are less susceptible to the effects of the S373P substitution.

Class 5 comprises the NAbs whose binding affinities exhibit the lowest susceptibility to the emergence of new variants among all RBD-targeting NAbs. Although the number of documented cases remains relatively low, it is noteworthy that, regardless of their original affinity for the Wuhan variant, none of these NAbs lose their binding capability. Within each of the two subclasses, a pair of NAbs shows variation in their interaction strength with the RBD, shifting between potent and super potent binders across the Omicron variant lineage (Figure 9-(5A,B))^{51,55-57}. However, no changes are observed in the interacting residues,

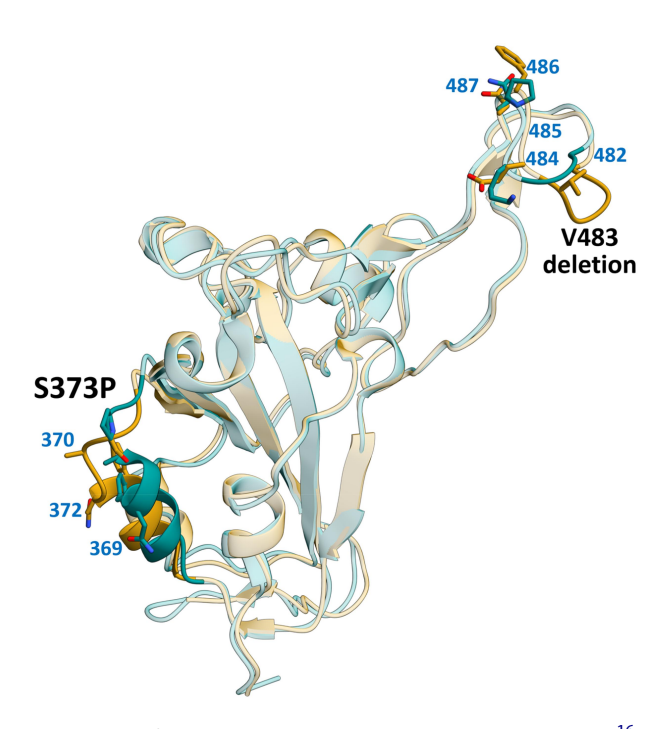


Figure 10. Comparison of RBD structures from the Wuhan variant (golden, PDB ID $6m0j^{16}$ and the Omicron JN.1 variant (teal, PDB ID 9kud⁵⁴), both solved in complex with hACE2. Two main regions of structural variation are evident: (i) the S373P substitution, fixed in Omicron variants, which repositions helix α_3 (RMSD 2.0 Å) and perturb the interaction with class 4 NAbs, and (ii) the V483 deletion, present since the Omicron BA.2.86 lineage, which rearranges the tip of the loop defined by the C480–C488 disulfide bond (Wuhan numbering), affecting the interaction zone with subclass 1B and class 2 NAbs. Excluding these regions, the RMSD between the two structures is 0.9 Å. Blue numbers indicate hotspot residues near structural perturbation regions.



whether hotspots or non-hotspots, indicating that the observed affinity differences are due to long-range conformational effects caused by substitutions outside the regions characteristic of subclasses 5A and 5B.

NAb recognition of RBD hotspots partially overlaps with in-silico epitope prediction

To evaluate how well in silico tools predict hotspot residues (frequency > 0.6) within RBD variants, a comparison of the experimentally identified hotspots was performed with in-silico epitope predictions using the BepiPred-2.0, -3.0 and the Kolaskar-Tongaonkar computational tools. The analysis assessed both potentially antigenic residues and those predicted to be recognizable by B cells (Figure 11).

The analyzed RBD sequence comprised residues 330 to 518. B-cell epitope linear prediction by BepiPred-2.0 identified three antigenic regions: the first is composed of the 357-375 residue range, of which only five were recognized by NAbs from classes 4A, 4B, and 5B. The second region, spanning residues 431 to 444, showed an overlap in five residues recognized by NAbs from classes 3A and 3B. The third region, located between residues 473 and 483, included seven residues recognized by NAbs from subclasses 1A, 1B, 2A, and 2B. In total, 17 of the residues predicted as B-cell epitopes overlapped with NAb-recognized residues, representing a concordance of 40.5% with the hotspot residues recognized by any of the NAb subclasses analyzed.

The discontinuous B-cell epitope prediction by BepiPred-3.0 increases the number of identified regions to 13, recognizing 56 residues at the RBD that are also recognized by NAbs. Particularly, regions from 354-357 recognized by NAbs from subclasses 2B, 5A, and 5B, 369-370 and 374,375 by 4A and 4B, and regions from 486-493 and 498 to 505 recognized by subclasses 1A, 1B, 2A, and 3B, were well predicted. This prediction allows identification of 11 of the 14 hotspot residues in the RBS region (Figure 11). Overall, Bepipred -3.0 predicted 27 amino acids that do not interact with NAbs, and 24 amino acids that are recognized by NAbs.

Regarding antigenicity, five main regions were identified. The first region, spanning residues 358 to 371, corresponded with two residues recognized by subclass 4B NAbs. The second region, encompassing residues 373 to 400, exhibited concordance in 10 residues recognized by subclasses 4A and 4B, as well as one additional residue recognized by subclasses 5A and 5B. The third region, located between residues 420 and 434, included three residues recognized by subclasses 1A and 5A. The fourth region, comprising residues 451 to 456, showed recognition of three residues by NAbs from subclasses 2A, 2B, 1A, and 1B. The fifth region, spanning residues 483 to 495, included 10 residues recognized by subclasses 1A, 1B, 2A, and 2B. Of the 72 residues predicted as antigenic, 28 hotspots were recognized by the NAbs assessed in this study, resulting in a prediction accuracy of 38.8%.

Additionally, it is noteworthy that 10 hotspot residues were recognized by one or more NAb subclasses evaluated in this study, but were not predicted by computational tools. Therefore, of the total 81 hotspot residues, 88% were successfully predicted by the in-silico analysis. Hotspot residues, such as those at positions 352, 416, 468, 470, 496, and 518, were not predicted as epitopes by any of the algorithms, despite being recognized by NAb subclasses 1A, 2B, 5A, and 5B. Upon reviewing the three-dimensional structure, the spatial proximity of these sites after protein folding suggests the presence of a conformational epitope, which the program may have failed to detect, an observation that has been reported in other studies⁵⁸.

It is essential to note that epitope prediction tools are frequently used as filters to direct research toward regions with higher immunogenic potential²⁸. However, the complex nature of antigen-Ab recognition demonstrates that much remains to be elucidated. Consequently, studies comparing in silico projections with their biological counterparts are essential for the continued improvement of Ab databases and for advancing the field of antibodyomics.

Discussion

In this study, we analyzed an extensive collection of structural data from anti-SARS-CoV-2 NAbs and Nbs, focusing on their three-dimensional interactions with the RBD of the S protein. Through detailed contact mapping, we propose a classification into five major classes and a total of 10 subclasses, which systematically organizes the interaction patterns according to distinct topographic regions, namely, the peak, the valley, the mesa, the short and long cliffs, and the inner and outer faces of the RBD. This framework enables the

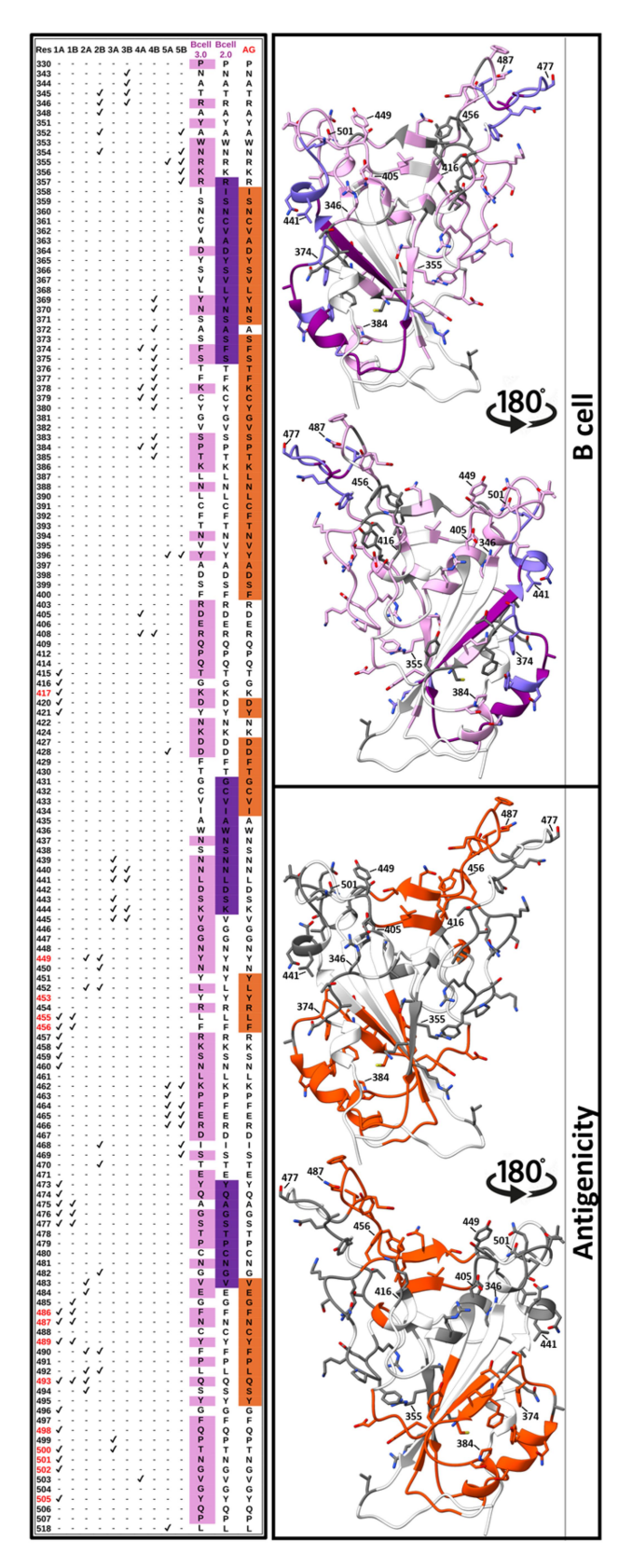


Figure 11. Antigenicity and B-cell epitope prediction compared to observed NAb hotspots in the RBD. On the left, the listed amino acids are either experimentally determined hotspots or have been predicted by at least one of the tested in silico tools. Check marks indicate experimentally observed NAb hotspots (frequency > 0.6) by subclass, while dashes indicate absence of residue usage as a hotspot. Residues forming part of the RBS are in red font. Pink and purple highlights indicate residues predicted as B-cell epitopes using BepiPred- 3.0^{30} and -2.0^{28} , respectively, while orange highlights represent antigenic peptide regions predicted with the Kolaskar & Tongaonkar method³¹. on the right side of the Figure, RBD structures are shown with predicted and non-predicted regions highlighted in color and gray, respectively, and matching residues between BepiPred-2.0 and -3.0 shown in violet (top right). Hotspot residues are shown in sticks. Residue numbers are included as reference.

identification of key surface features targeted by the humoral immune response. As previously reported, most NAbs found in the sera from infected or vaccinated individuals are directed toward the apical region of the RBD. According to our classification, these NAbs group primarily into subclasses 1A, 1B, or 2A. Notably, subclass 1A NAbs display highly consistent binding features, whereas other subclasses exhibit greater diversity in binding modes and contact interfaces.

We further compared affinity constants across NAb subclasses from the Wuhan through Omicron variants, identifying groups that retain high affinity despite the accumulation of viral mutations. Over time, an increasing number of high-affinity NAbs (K_D < 1 nM) have been reported to target peripheral regions of the RBD, such as the short and long cliffs. These NAbs, which often recognize cryptic epitopes, are classified into classes 3, 4, or 5. Our comprehensive analysis of subclass-specific affinity evolution reinforces the idea that both epitope location and the fitness of molecular contacts critically influence NAb sensitivity to Omicron variants. Although clear correlations are observed between hotspot substitutions and affinity losses in many cases, notable exceptions exist where substitutions outside hotspot regions result in significant weakening of binding. These observations highlight the structural and functional complexity of NAb–RBD interaction networks, cautioning against interpretations based solely on linear epitope overlap.

The accumulation of mutations during SARS-CoV-2 evolution has introduced important changes in the RBD, enabling the escape of more recent viral strains. Among these, only two mutations appear to have a clear impact on its folding pattern: the S373P substitution and the V483 deletion (Figure 10). The S373P substitution induces a local rearrangement that affects a reduced fraction of class 4 NAbs depending on their angle of approach, while leaving others largely unaffected. By contrast, structural and affinity data for subclass 1B and class 2 NAbs recognizing RBDs with the relative recent V483 deletion remain limited. However, giving binding modes in which V483 and adjacent residues are minimally or not contacted, a resilient behavior can be anticipated for NAbs such as 7F3 (subclass 1B), S2D106 and XGv282 (subclass 2A), and BD-744 and FC08 (subclass 2B). These cases illustrate how specific mutations can selectively alter the binding patterns of NAbs originally elicited against the Wuhan strain, while also underscoring structural determinants of NAb resilience in the context of viral escape.

One of the earliest systematic efforts to classify anti-RBD NAbs was by Barnes et al.⁵⁹, who defined four major classes based on the NAb's orientation relative to the RBD. Alternative classification schemes were also described (e.g., 60). Barnes et al. classified anti-SARS-CoV-2 NAbs into four structural classes: Class 1, VH3-53-encoded NAbs that block ACE2 and bind only "up" RBDs; Class 2, ACE2-blocking NAbs that bind both "up" and "down" RBDs and can contact adjacent RBDs; Class 3, NAbs that bind outside the ACE2 site and recognize both RBD conformations; and Class 4, NAbs that do not block ACE2 and bind only "up" RBDs. Due to its foundational nature and conceptual clarity, this classification became widely adopted, and many subsequent structural studies integrated newly solved NAbs into the original Barnes classes (Table SI-12^{61–68}). However, as the number of available structures has expanded, a broader diversity of binding modes has emerged, many of which do not fully conform to the initial four-class model. This led to the proposal of new NAbs groups, such as classes 5 and 6^{61,65,68,69}, to accommodate NAbs that target noncanonical or peripheral regions of the RBD. Despite these refinements, as sum https://ourworldindata.org/covid-deaths marized in Table SI-12, inconsistencies in NAb classification persist. In some instances, structurally similar NAbs have been placed in different classes, while NAbs with clearly distinct binding modes have been grouped together. For instance, the NAbs grouped as class 6 by Rouet et al. and Mazigi et al.⁶⁵ are found dispersed across our subclasses 2A, 2B and 5B.

A similar issue arises with alternative classification systems, such as the one proposed by Jiang et al.⁷⁰, who defined 23 epitopic sites on the RBD by segmenting it according to secondary structure elements and analyzing recognition frequency across a dataset of 340 NAbs and 83 Nbs. Using principal component analysis, they grouped these NAbs into 33 clusters, each reflecting a different spatial mode of epitope engagement. However, this level of granularity tends to over-segment NAb groupings. For example, within our own dataset, we identified 86 NAbs that conform to subclass 1A, all of which display a notably consistent binding mode. In contrast, the Jiang classification distributes subclass 1A NAbs across 10 different clusters. Furthermore, some of these 10 clusters also include NAbs that, according to our topological classification, belong to completely different subclasses, highlighting a lack of structural coherence. Similar mismatches are observed when comparing our classification to other previously proposed schemes (Table SI-13, ^{57,60,70-74}), underscoring the need for a harmonized, quantitative, and



topologically consistent framework that more accurately captures the structural organization of anti-RBD NAb repertoires.

In our dataset, no Nbs were identified within subclasses 1A or 3A. The majority of Nbs clustered within subclass 2A, which corresponds to an epitope region that remains permanently solvent-exposed, facilitating stable binding. Additional Nbs were distributed across classes 2–5, in agreement with their proposed ability to reach cryptic or recessed sites on the RBD^{70,75}.

Notably, the frequency with which NAbs target specific epitopes does not necessarily correlate with the extent of somatic hypermutation, yet the Ab repertoire continues to diversify over time. This evolving pattern of recognition increasingly extends beyond classical immunodominant regions to include cryptic epitopes, such as the long and short cliffs and the lower portions of the RBD's inner face. These sites, notable for their low mutation rates across viral variants, represent attractive targets for therapeutic intervention. Our structural analysis further revealed that recurrent binding motifs found in human NAbs often diverge from those predicted by computational models. By mapping hotspot residues and their interactions across SARS-CoV-2 variants, we identify highly targeted regions on the RBD (Figures 2–7).

Our classification led us to revisit the antigenic landscape of the SARS-CoV-2 S glycoprotein RBD, identifying key candidate epitopes. Unlike BepiPred -3.0, our topographically driven framework captures additional epitope sites, preserves structural consistency, and extends existing classifications to encompass noncanonical epitopes, thereby enabling quantitative interpretation of antibody binding across SARS-CoV -2 variants. Our analysis revealed antigenic surfaces including the outer face, the long cliff, the valley, the mesa, and the RBS, thus uncovering antigenic epitopes that are bioinformatically unpredicted, particularly those exposed in the open conformation of the S protein. Similarly, although the Kolaskar-Tongaonkar method detects some accessible regions (e.g., the peak, the valley, and the inner face) in the closed state, we identified critical antigenic regions in cryptic sites such as the short cliff. In the case of Nbs, consistent with previous studies, our database revealed a relative underrepresentation (~42%) of those recognizing fully exposed regions (such as those grouped in subclasses 2A and 3A) compared to those binding cryptic or partially accessible regions of the RBD in the closed or partially closed conformations of the S protein⁷⁶. This biased distribution may be influenced by their unusually long CDR3 loops and compact size, which enable them to access recessed or otherwise occluded antigenic surfaces that are less accessible to conventional Abs^{70,75}. Overall, our findings underscore the need for in-depth studies of epitope–paratope interactions based on structural data to achieve comprehensive epitope mapping.

Classes 4 and 5 NAbs stand out as promising candidates for therapeutic development because they target cryptic or poorly accessible epitopes of the RBD that remain largely unaffected by hotspot mutations accumulated during the evolution of Omicron variants. Together, these NAbs, as well as related Nbs, exhibit remarkable therapeutic potential and are promising tools for prophylactic strategies, since their activity is less likely to be compromised by viral evolution.

Our topologically driven framework, grounded in a hotspot basis, preserves structural consistency, integrates prior classifications, and extends them to include new NAbs targeting noncanonical or peripheral epitopes. By emphasizing the correspondence between epitope topology and hotspot residues, this approach provides a clearer and less ambiguous grouping of NAbs. It further allows for the systematic interpretation of functional features, such as competition or noncompetition with hACE2, binding to RBD in the up and/or down states, and correlation with regions of higher or lower sequence variability. Importantly, it also enables the quantitative evaluation of binding tolerance across SARS-CoV-2 variants, from Wuhan to Omicron, highlighting subclasses that retain high-affinity interactions despite accumulating mutations. By unifying previous schemes, rationalizing differential neutralization, and delineating functionally relevant epitopes, our classification delivers a practical, harmonized, and structurally coherent strategy for interpreting NAb repertoires and guiding therapeutic and vaccine design against current and future SARS-CoV-2 variants.

Concluding remarks

There is a growing global interest in understanding the immune response to SARS-CoV-2, which has led to significant advances in our knowledge of B and T cell adaptation following infection or



vaccination. These advances have deepened our understanding of how NAb production and interaction with the virus's key target, the RBD, are regulated. Such understanding has proven valuable for the development of preventive and therapeutic strategies against Sarbecovirus. However, a systematic and well-defined classification of NAbs that recognize the RBD of the SARS-CoV-2 S protein is essential for the design of more precise and robust neutralization strategies, particularly in the face of emerging variants with potential global health impact. Structural categorization of NAbs not only highlights vulnerable regions of the virus, but also allows for the anticipation of viral escape mechanisms and supports the rational development of vaccines and monoclonal NAb therapies.

Acknowledgments

FDM-S, JAR-C and AD-V are doctoral students from Programa de Doctorado en Ciencias Bioquímicas, Universidad Nacional Autónoma de México (UNAM), and received a fellowship from Secretaría de Ciencia, Humanidades, Tecnología e Innovación (SECIHTI), CVU: 887520, 1019311 and 1009458, respectively. PM-E received a postdoctoral fellowship from SECIHTI, CVU: 204635. NAV-C and MAT-R thank the sabbatical fellowship to "Programa de Apoyos para la Superación del Personal Académico" PASPA-DGAPA- UNAM. The authors thank M. Sc. Itandehui Betanzo, Dr. Oscar González-Davis, M. Eng. Martha Elena Carrasco Fuentes, and M. Comm. Sonia Olguín García, M.I.A. María Magdalena Aguilar Araiza, Mtra. en Admón. Gladys Edith Cortés Romero, and M. A. Mario Trejo Loyo for their technical support. We acknowledge the use of Miztli (LANCAD-UNAM-DGTIC-213) high-performance computing resources (EG-H).

Disclosure statement

No potential conflict of interest was reported by the author(s).

Funding

This work was supported by Programa de Apoyo a Proyectos de Investigación e Innovación Tecnológica, Universidad Nacional Autónoma de México [IV201220, IN209624], and Secretaría de Ciencia, Humanidades, Tecnología e Innovación (SECIHTI) [MAT-R: CF-2023-I-1248 and NAV-C: CF-2023-I-1549]. The funders had no role in data collection and analysis, publication decisions, or manuscript preparation.

ORCID

Luis Fernando Cofas-Vargas http://orcid.org/0000-0001-5603-1437 Paola Mendoza-Espinosa http://orcid.org/0000-0003-1447-8040 Fernando D. Montalvo-Sandoval http://orcid.org/0009-0008-7114-4139 Saumel Pérez-Rodríguez http://orcid.org/0000-0003-3852-008X Jesús Antonio Rauda-Ceja http://orcid.org/0009-0008-9283-7006 Pablo Hernández-Peralta http://orcid.org/0000-0002-0399-3023 Adrián Durán-Vargas http://orcid.org/0009-0007-8836-1765 Mauricio A. Trujillo-Roldán (b) http://orcid.org/0000-0002-7497-4452 Norma A. Valdez-Cruz (b) http://orcid.org/0000-0002-8581-1173 Enrique García-Hernández http://orcid.org/0000-0003-4561-4973

Artificial intelligence (AI)

Artificial intelligence tools (such as ChatGPT) were used to assist in the language editing and polishing of this manuscript. The authors reviewed and approved all final content.

References

1. Mathieu E, Ritchie H, Rodés-Guirao L, Appel C, Gavrilov D, Giattino C, Hasell J, Macdonald B, Dattani SBeltekian D, et al. Coronavirus (COVID-19) deaths. Our World Data. 2020. https://ourworldindata. org/covid-deaths



- 2. Valdez-Cruz NA, García-Hernández E, Espitia C, Cobos-Marín L, Altamirano C, Bando-Campos CG, Cofas-Vargas LF, Coronado-Aceves EW, González-Hernández RAHernández-Peralta P, et al. Integrative overview of antibodies against SARS-CoV-2 and their possible applications in COVID-19 prophylaxis and treatment. Microb Cell Fact. 2021;20(1):88. doi: 10.1186/s12934-021-01576-5.
- 3. World Health Organization. Tracking SARS-CoV-2 variants. 2025 [cited 2025 Jul 28]; https://www.who.int/activities/tracking-SARS-CoV-2-variants.
- 4. Chen R, Zhang X, Yuan Y, Deng X, Wu B, Xi Z, Wang G, Lin Y, Li RWang X, et al. Development of receptor binding domain (RBD)-conjugated nanoparticle vaccines with broad neutralization against SARS-CoV-2 Delta and other variants. Adv Sci. 2022;9(11). doi: 10.1002/advs.202105378.
- 5. Wang X, Rcheulishvili N, Cai J, Liu C, Xie F, Hu X, Yang N, Hou M, Papukashvili DHe Y, et al. Development of DNA vaccine candidate against SARS-CoV-2. Viruses. 2022;14(5):1049. doi: 10.3390/v14051049.
- 6. U.S. Food and Drug Administration. Covid19 vaccines for 2024–2025. https://www.fda.gov/emergency-preparedness-and-response/coronavirus-disease-2019-covid-19/covid-19-vaccines-2024-20252024;.
- 7. Centers for Disease Control and Prevention. Overview of COVID19 vaccines and vaccination. https://www.cdc.gov/covid/hcp/vaccine-considerations/overview.html2025;.
- 8. Sternberg A, Naujokat C. Structural features of coronavirus SARS-CoV-2 spike protein: targets for vaccination. Life Sci. 2020;257:118056. doi: 10.1016/j.lfs.2020.118056.
- 9. Harvey WT, Carabelli AM, Jackson B, Gupta RK, Thomson EC, Harrison EM, Ludden C, Reeve R, Rambaut APeacock SJ, et al. SARS-CoV-2 variants, spike mutations and immune escape. Nat Rev Microbiol. 2021;19(7):409–424. doi: 10.1038/s41579-021-00573-0.
- 10. Pastorio C, Noettger S, Nchioua R, Zech F, Sparrer KMJ, Kirchhoff F. Impact of mutations defining SARS-CoV-2 Omicron subvariants BA.2.12.1 and BA.4/5 on spike function and neutralization. iScience. 2023;26(11):108299. doi: 10.1016/j.isci.2023.108299.
- 11. World Health Organization. Risk evaluation for SARSCoV2 variant under monitoring: XFG (Technical Advisory Group on Virus Evolution report). 2025 [cited 2025 Jul 28]; https://www.who.int/publications/m/item/risk-evaluation-for-sars-cov-2-variant-under-monitoring-xfg.
- 12. Gur M, Taka E, Yilmaz SZ, Kilinc C, Aktas U, Golcuk M. Conformational transition of SARS-CoV-2 spike glycoprotein between its closed and open states. J Chem Phys. 2020;153(7):075101. doi: 10.1063/5.0011141.
- 13. Shah M, Ahmad B, Choi S, Woo HG. Mutations in the SARS-CoV-2 spike RBD are responsible for stronger ACE2 binding and poor anti-SARS-CoV mAbs cross-neutralization. Comput Struct Biotechnol J. 2020;18:3402–3414. doi: 10.1016/j.csbj.2020.11.002.
- 14. Wang Q, Guo Y, Mellis IA, Wu M, Mohri H, Gherasim C, Valdez R, Purpura LJ, Yin MTGordon A, et al. Antibody evasiveness of SARS-CoV-2 subvariants KP.3.1.1 and XEC. Cell Rep. 2025;44(4):115543. doi: 10.1016/j.celrep.2025.115543.
- 15. Dokainish HM, Re S, Mori T, Kobayashi C, Jung J, Sugita Y. The inherent flexibility of receptor binding domains in SARS-CoV-2 spike protein. Elife. 2022;11:11. doi: 10.7554/eLife.75720.
- 16. Lan J, Ge J, Yu J, Shan S, Zhou H, Fan S, Zhang Q, Shi X, Wang QZhang L, et al. Structure of the SARS-CoV-2 spike receptor-binding domain bound to the ACE2 receptor. Nature. 2020;581(7807):215–220. doi: 10.1038/s41586-020-2180-5.
- 17. Hastie KM, Li H, Bedinger D, Schendel SL, Dennison SM, Li K, Rayaprolu V, Yu X, Mann CZandonatti M, et al. Defining variant-resistant epitopes targeted by SARS-CoV-2 antibodies: a global consortium study. Science (1979). 2021;374(6566):472–478. doi: 10.1126/science.abh2315.
- 18. Qi H, Liu B, Wang X, Zhang L. The humoral response and antibodies against SARS-CoV-2 infection. Nat Immunol. 2022;23(7):1008–1020. doi: 10.1038/s41590-022-01248-5.
- 19. Chan CEZ, Seah SGK, Chye DH, Massey S, Torres M, Lim APC, Wong SKK, Neo JJY, Wong PSLim JH, et al. The Fc-mediated effector functions of a potent SARS-CoV-2 neutralizing antibody, SC31, isolated from an early convalescent COVID-19 patient, are essential for the optimal therapeutic efficacy of the antibody. PLOS ONE. 2021;16(6):e0253487. doi: 10.1371/journal.pone.0253487.
- 20. Zhang A, Stacey HD, D'Agostino MR, Tugg Y, Marzok A, Miller MS. Beyond neutralization: Fc-dependent antibody effector functions in SARS-CoV-2 infection. Nat Rev Immunol. 2023;23(6):381–396. doi: 10.1038/s41577-022-00813-1.
- 21. Barnes CO, West AP, Huey-Tubman KE, Hoffmann MAG, Sharaf NG, Hoffman PR, Koranda N, Gristick HB, Gaebler CMuecksch F, et al. Structures of human antibodies bound to SARS-CoV-2 spike reveal common epitopes and recurrent features of antibodies. Cell. 2020;182(4):828–842.e16. doi: 10.1016/j.cell.2020.06.025.
- 22. Walls AC, Park Y-J, Tortorici MA, Wall A, McGuire AT, Veesler D. Structure, function, and antigenicity of the SARS-CoV-2 spike glycoprotein. Cell. 2020;181(2):281–292.e6. doi: 10.1016/j.cell.2020.02.058.
- 23. Wrapp D, Wang N, Corbett KS, Goldsmith JA, Hsieh C-L, Abiona O, Graham BS, McLellan JS. Cryo-EM structure of the 2019-nCoV spike in the prefusion conformation. Science (1979). 2020;367(6483):1260–1263. doi: 10.1126/science.abb2507.
- 24. Wołek K, Gómez-Sicilia À, Cieplak M. Determination of contact maps in proteins: a combination of structural and chemical approaches. J Chem Phys. 2015;143(24):143. doi: 10.1063/1.4929599.



- 25. Moreira RA, Chwastyk M, Baker JL, Guzman HV, Poma AB. Quantitative determination of mechanical stability in the novel coronavirus spike protein. Nanoscale. 2020;12(31):16409-16413. doi: 10.1039/D0NR03969A.
- 26. Tsai J, Taylor R, Chothia C, Gerstein M. The packing density in proteins: standard radii and volumes 1 ledited by J. M. Thornton. J Mol Biol. 1999;290(1):253-266. doi: 10.1006/jmbi.1999.2829.
- 27. Crooks GE, Hon G, Chandonia J-M, Brenner SE. WebLogo: a sequence logo generator. Genome Res. 2004;14 (6):1188-1190. doi: 10.1101/gr.849004.
- 28. Jespersen MC, Peters B, Nielsen M, Marcatili P. Bepipred-2.0: improving sequence-based B-cell epitope prediction using conformational epitopes. Nucleic Acids Res. 2017;45(W1):W24-9. doi: 10.1093/nar/gkx346.
- 29. Saha S, Raghava GPS. Prediction of continuous B-cell epitopes in an antigen using recurrent neural network. Proteins Struct Funct Bioinf. 2006;65(1):40–48. doi: 10.1002/prot.21078.
- 30. Clifford JN, Høie MH, Deleuran S, Peters B, Nielsen M, Marcatili P. Bepipred -3.0: improved B-cell epitope prediction using protein language models. Protein Sci. 2022;31(12):31. doi: 10.1002/pro.4497.
- 31. Kolaskar AS, Tongaonkar PC. A semi-empirical method for prediction of antigenic determinants on protein antigens. FEBS Lett. 1990;276(1-2):172-174. doi: 10.1016/0014-5793(90)80535-Q.
- 32. Muecksch F, Weisblum Y, Barnes CO, Schmidt F, Schaefer-Babajew D, Wang Z, Julio JC, Flyak AI, DeLaitsch ATHuey-Tubman KE, et al. Affinity maturation of SARS-CoV-2 neutralizing antibodies confers potency, breadth, and resilience to viral escape mutations. Immunity. 2021;54(8):1853-1868.e7. doi: 10.1016/j. immuni.2021.07.008.
- 33. Yao H, Sun Y, Deng YQ, Wang N, Tan Y, Zhang NN, Li XF, Kong C, Xu YPChen Q, et al. Rational development of a human antibody cocktail that deploys multiple functions to confer pan-SARS-CoVs protection. Cell Res. 2021;31(1):25-36. doi: 10.1038/s41422-020-00444-v.
- 34. Bracken CJ, Lim SA, Solomon P, Rettko NJ, Nguyen DP, Zha BS, Schaefer K, Byrnes JR, Zhou JLui I, et al. Biparatopic and multivalent VH domains block ACE2 binding and neutralize SARS-CoV-2. Nat Chem Biol. 2021;17(1):113-121. doi: 10.1038/s41589-020-00679-1.
- 35. Hong J, Kwon HJ, Cachau R, Chen CZ, Butay KJ, Duan Z, Li D, Ren H, Liang TZhu J, et al. Dromedary camel nanobodies broadly neutralize SARS-CoV-2 variants. Proceedings of the National Academy of Sciences; 2022. p. 119.
- 36. Lv Z, Deng Y-Q, Ye Q, Cao L, Sun C-Y, Fan C, Huang W, Sun S, Sun YZhu L, et al. Structural basis for neutralization of SARS-CoV-2 and SARS-CoV by a potent therapeutic antibody. Science (1979). 2020;369 (6510):1505-1509. doi: 10.1126/science.abc5881.
- 37. Xiang Y, Huang W, Liu H, Sang Z, Nambulli S, Tubiana J, Williams KL, Duprex WP, Schneidman-Duhovny DWilson IA, et al. Superimmunity by pan-sarbecovirus nanobodies. Cell Rep. 2022;39(13):39. doi: 10.1016/j. celrep.2022.111004.
- 38. Liu H, Wu L, Liu B, Xu K, Lei W, Deng J, Rong X, Du P, Wang L, Wang D, et al. Two pan-SARS-CoV-2 nanobodies and their multivalent derivatives effectively prevent Omicron infections in mice. Cell Rep Med. 2023;4(2):100918. doi: 10.1016/j.xcrm.2023.100918.
- 39. Yao H, Cai H, Li T, Zhou B, Qin W, Lavillette D, Li D. A high-affinity RBD-targeting nanobody improves fusion partner's potency against SARS-CoV-2. PLOS Pathog. 2021;17(3):e1009328. doi: 10.1371/journal.ppat.1009328
- 40. Li C, Zhan W, Yang Z, Tu C, Hu G, Zhang X, Song W, Du S, Zhu YHuang K, et al. Broad neutralization of SARS-CoV-2 variants by an inhalable bispecific single-domain antibody. Cell. 2022;185(8):1389-1401.e18. doi: 10.1016/j.cell.2022.03.009.
- 41. Kim S, Liu Y, Ziarnik M, Seo S, Cao Y, Zhang XF, Im W. Binding of human ACE2 and RBD of Omicron enhanced by unique interaction patterns among SARS-CoV-2 variants of concern. J Comput Chem. 2023;44 (4):594-601. doi: 10.1002/jcc.27025.
- 42. Barton MI, MacGowan SA, Kutuzov MA, Dushek O, Barton GJ, van der Merwe PA. Effects of common mutations in the SARS-CoV-2 spike RBD and its ligand, the human ACE2 receptor on binding affinity and kinetics. Elife. 2021;10:10. doi: 10.7554/eLife.70658.
- 43. Laffeber C, de Koning K, Kanaar R, Lebbink JHG. Experimental evidence for enhanced receptor binding by rapidly spreading SARS-CoV-2 variants. J Mol Biol. 2021;433(15):167058. doi: 10.1016/j.jmb.2021.167058.
- 44. Lin S, Chen Z, Zhang X, Wen A, Yuan X, Yu C, Yang J, He B, Cao Y, Lu G. Characterization of SARS-CoV-2 Omicron spike RBD reveals significantly decreased stability, severe evasion of neutralizing-antibody recognition but unaffected engagement by decoy ACE2 modified for enhanced RBD binding. Signal Transduct Target Ther. 2022;7(1):56. doi: 10.1038/s41392-022-00914-2.
- 45. Piplani S, Singh PK, Winkler DA, Petrovsky N. In silico comparison of SARS-CoV-2 spike protein-ACE2 binding affinities across species and implications for virus origin. Sci Rep. 2021;11(1):13063. doi: 10.1038/ s41598-021-92388-5.
- 46. Nguyen HL, Lan PD, Thai NQ, Nissley DA, O'Brien EP, Li MS. Does SARS-CoV-2 bind to human ACE2 more strongly than does SARS-CoV? J Phys Chem B. 2020;124(34):7336-7347. doi: 10.1021/acs.jpcb.0c04511.
- 47. Li L, Liao H, Meng Y, Li W, Han P, Liu K, Wang Q, Li D, Zhang YWang L, et al. Structural basis of human ACE2 higher binding affinity to currently circulating Omicron SARS-CoV-2 sub-variants BA.2 and BA.1.1. Cell. 2022;185(16):2952-2960.e10. doi: 10.1016/j.cell.2022.06.023.
- 48. Huan X, Zhan J, Gao H. Research progress of spike protein mutation of SARS-CoV-2 mutant strain and antibody development. Front Immunol. 2024;15:1407149. doi: 10.3389/fimmu.2024.1407149.



- 49. Jian F, Wec AZ, Feng L, Yu Y, Wang L, Wang P, Yu L, Wang J, Hou JBerrueta DM, et al. Viral evolution prediction identifies broadly neutralizing antibodies to existing and prospective SARS-CoV-2 variants. Nat Microbiol. 2025;10:2003–2017. doi: 10.1038/s41564-025-02030-7.
- 50. Brouwer PJM, Caniels TG, van der Straten K, Snitselaar JL, Aldon Y, Bangaru S, Torres JL, Okba NMA, Claireaux MKerster G, et al. Potent neutralizing antibodies from COVID-19 patients define multiple targets of vulnerability. Science (1979). 2020;369(6504):643–650. doi: 10.1126/science.abc5902.
- 51. He Q, Wu L, Xu Z, Wang X, Xie Y, Chai Y, Zheng A, Zhou J, Qiao SHuang M, et al. An updated atlas of antibody evasion by SARS-CoV-2 Omicron sub-variants including BQ.1.1 and XBB. Cell Rep Med. 2023;4(4):100991. doi: 10.1016/j.xcrm.2023.100991.
- 52. He P, Liu B, Gao X, Yan Q, Pei R, Sun J, Chen Q, Hou R, Li ZZhang Y, et al. SARS-CoV-2 Delta and Omicron variants evade population antibody response by mutations in a single spike epitope. Nat Microbiol. 2022;7 (10):1635–1649. doi: 10.1038/s41564-022-01235-4.
- 53. Yan Q, Gao X, Liu B, Hou R, He P, Ma Y, Zhang Y, Li ZChen Q, et al. Antibodies utilizing VL6-57 light chains target a convergent cryptic epitope on SARS-CoV-2 spike protein and potentially drive the genesis of Omicron variants. Nat Commun. 2024;15(1):15. doi: 10.1038/s41467-024-51770-3.
- 54. Wang C, Nan X, Deng Y, Fan S, Lan J. Cross-species recognition of squirrel ACE2 by the receptor binding domains of SARS-CoV-2, RaTG13, PCoV-GD and PCoV-GX. Structure. 2025;33(10):1750–1759.e2. doi: 10.1016/j.str.2025.07.003.
- 55. Jensen JL, Sankhala RS, Dussupt V, Bai H, Hajduczki A, Lal KG, Chang WC, Martinez EJ, Peterson CEGolub ES, et al. Targeting the spike receptor binding domain class V cryptic epitope by an antibody with pan-sarbecovirus activity. J Virol. 2023;97(7). doi: 10.1128/jvi.01596-22.
- 56. Tong Z, Tong J, Lei W, Xie Y, Cui Y, Jia G, Li S, Zhang Z, Cheng ZXing X, et al. Deciphering a reliable synergistic bispecific strategy of rescuing antibodies for SARS-CoV-2 escape variants, including BA.2.86, EG.5.1, and JN.1. Cell Rep. 2024;43(6):43. doi: 10.1016/j.celrep.2024.114338.
- 57. Rao X, Zhao R, Tong Z, Guo S, Peng W, Liu K, Li S, Wu L, Tong JChai Y, et al. Defining a de novo non-RBM antibody as RBD-8 and its synergistic rescue of immune-evaded antibodies to neutralize Omicron SARS-CoV-2. Proc Natl Acad Sci USA. 2023;120(52):120. doi: 10.1073/pnas.2314193120.
- 58. Elko EA, Nelson GA, Mead HL, Kelley EJ, Carvalho ST, Sarbo NG, Harms CE, Le Verche V, Cardoso AAEly JL, et al. COVID-19 vaccination elicits an evolving, cross-reactive antibody response to epitopes conserved with endemic coronavirus spike proteins. Cell Rep. 2022;40(1):111022. doi: 10.1016/j.celrep.2022.111022.
- 59. Barnes CO, Jette CA, Abernathy ME, Dam KMA, Esswein SR, Gristick HB, Malyutin AG, Sharaf NG, Huey-Tubman KELee YE, et al. SARS-CoV-2 neutralizing antibody structures inform therapeutic strategies. Nature. 2020;588(7839):682–687. doi: 10.1038/s41586-020-2852-1.
- 60. Piccoli L, Park YJ, Tortorici MA, Czudnochowski N, Walls AC, Beltramello M, Silacci-Fregni C, Pinto D, Rosen LEBowen JE, et al. Mapping neutralizing and immunodominant sites on the SARS-CoV-2 spike receptor-binding domain by structure-guided high-resolution serology. Cell. 2020;183(4):1024–1042.e21. doi: 10.1016/j.cell.2020.09.037.
- 61. Cui Z, Liu P, Wang N, Wang L, Fan K, Zhu Q, Wang K, Chen R, Feng RJia Z, et al. Structural and functional characterizations of infectivity and immune evasion of SARS-CoV-2 Omicron. Cell. 2022;185(5):860–871.e13. doi: 10.1016/j.cell.2022.01.019.
- 62. Almagro JC, Mellado-Sánchez G, Pedraza-Escalona M, Pérez-Tapia SM. Evolution of anti-SARS-CoV-2 therapeutic antibodies. Int J Mol Sci. 2022;23(17):9763. doi: 10.3390/ijms23179763.
- 63. Mittal A, Khattri A, Verma V. Structural and antigenic variations in the spike protein of emerging SARS-CoV-2 variants. PLOS Pathog. 2022;18(2):e1010260. doi: 10.1371/journal.ppat.1010260.
- 64. Rouet R, Henry JY, Johansen MD, Sobti M, Balachandran H, Langley DB, Walker GJ, Lenthall H, Jackson JUbiparipovic S, et al. Broadly neutralizing SARS-CoV-2 antibodies through epitope-based selection from convalescent patients. Nat Commun. 2023;14(1):14. doi: 10.1038/s41467-023-36295-5.
- 65. Jia Z, Wang K, Xie M, Wu J, Hu Y, Zhou Y, Yisimayi A, Fu W, Wang LLiu P, et al. A third dose of inactivated vaccine augments the potency, breadth, and duration of anamnestic responses against SARS-CoV-2. Protein Cell. 2024;15(12):930–937. doi: 10.1093/procel/pwae033.
- 66. Zhang T, Yang D, Tang L, Hu Y. Current development of severe acute respiratory syndrome coronavirus 2 neutralizing antibodies (Review). Mol Med Rep. 2024;30(2):148. doi: 10.3892/mmr.2024.13272.
- 67. Zhao X, Qiu T, Huang X, Mao Q, Wang Y, Qiao R, Li J, Mao T, Wang YCun Y, et al. Potent and broadly neutralizing antibodies against sarbecoviruses induced by sequential COVID-19 vaccination. Cell Discov. 2024;10(1):10. doi: 10.1038/s41421-024-00648-1.
- 68. Mazigi O, Langley DB, Henry JY, Burnett DL, Sobti M, Walker GJ, Rouet R, Balachandran H, Lenthall HJackson J, et al. Affinity maturation endows potent activity onto class 6 SARS-CoV-2 broadly neutralizing antibodies. Proc Natl Acad Sci USA. 2025;122(1):122. doi: 10.1073/pnas.2417544121.
- 69. Rouet R, Mazigi O, Walker GJ, Langley DB, Sobti M, Schofield P, Lenthall H, Jackson J, Ubiparipovic SHenry JY, et al. Potent SARS-CoV-2 binding and neutralization through maturation of iconic SARS-CoV-1 antibodies. Mabs. 2021;13(1). doi: 10.1080/19420862.2021.1922134.



- 70. Jiang J, Boughter CT, Ahmad J, Natarajan K, Boyd LF, Meier-Schellersheim M, Margulies DH. SARS-CoV-2 antibodies recognize 23 distinct epitopic sites on the receptor binding domain. Commun Biol. 2023;6(1):953. doi: 10.1038/s42003-023-05332-w.
- 71. Starr TN, Greaney AJ, Hannon WW, Loes AN, Hauser K, Dillen JR, Ferri E, Farrell AG, Dadonaite BMccallum M, et al. Shifting mutational constraints in the SARS-CoV-2 receptor-binding domain during viral evolution. Science(1979). 2022;377(6604):420–424. doi: 10.1126/science.abo7896.
- 72. Xue J. Tao S. Epitope analysis of anti-SARS-CoV-2 neutralizing antibodies. Curr Med Sci. 2021;41(6):1065–1074. doi: 10.1007/s11596-021-2453-8.
- 73. Yuan M, Liu H, Wu NC, Lee C-C, Zhu X, Zhao F, Huang D, Yu W, Hua YTien H, et al. Structural basis of a shared antibody response to SARS-CoV-2. Science (1979). 2020;369(6507):1119–1123. doi: 10.1126/science.abd2321.
- 74. Cao Y, Jian F, Wang J, Yu Y, Song W, Yisimayi A, Wang J, An R, Chen XZhang N, et al. Imprinted SARS-CoV-2 humoral immunity induces convergent Omicron RBD evolution. Nature. 2022;614:521–529. doi: 10.1038/s41586-022-05644-7.
- 75. Arbabi-Ghahroudi M. Camelid single-domain antibodies: promises and challenges as lifesaving treatments. Int J Mol Sci. 2022;23(9):5009. doi: 10.3390/ijms23095009.
- 76. Revets H, De Baetselier P, Muyldermans S. Nanobodies as novel agents for cancer therapy. Expert Opin Biol Ther. 2005;5(1):111–124. doi: 10.1517/14712598.5.1.111.